A Measurement of the Mixing Parameter $\sin^2(2\theta_{13})$ at Daya Bay

CHENG-JU LIN, YASUHIRO NAKAJIMA, J. PEDRO OCHOA,
PATRICK TSANG AND HENOCH WONG

Lawrence Berkeley National Laboratory

March 8, 2012

Abstract

We report a measurement of the oscillation parameter $\sin^2(2\theta_{13})$ using data from December 24, 2011 to February 17, 2012, based on a relative IBD rate measurement between the near and far site ADs. Assuming normal neutrino mass hierarchy, the best fit value is $\sin^2(2\theta_{13}) = 0.0932^{+0.0159}_{-0.0160}$(stat.)$\pm0.0059$(syst.). For the inverted mass hierarchy scenario, the central value shifts by a negligible amount of 0.6%. The null hypothesis of $\sin^2(2\theta_{13}) = 0$ is excluded using a 100-million toy MC sample with a significance of greater than 5σ.

Significant changes from previous revision:

- A small bug in the toy MC was fixed; the slight slope in the Feldman-Cousins contours is now gone (see Section 9.2.2).The confidence intervals changed minimally.

- More information added to the section about the oscillation probability calculation (see Section 6.1).

- A cross-check was done to make sure the time-dependence is being properly handled (see Section 6.2.2).

- A cross-check on the number of degrees of freedom was performed (see end of Section 8.1).

1 Introduction

This note contains a detailed description of our effort to extract the θ_{13} mixing angle through a relative measurement of the near and far AD rates. Specifically, our methodology consists in predicting the far AD rates based on the measured near AD rates as a function of θ_{13} and finding the value that best fits the data.

Our choice of methodology obeys to a number of reasons, mainly related to the advantages inherent to performing a completely relative analysis. By definition, one need not worry about absolute quantities whenever performing this type of analysis. In our case this results in increased simplicity, as quantities that are not directly observable such as, for instance, the absolute IBD cross-sections and the detection efficiencies, do not play a direct role. But perhaps the most appealing advantage is that all of the correlated systematic errors, defined as those effects that

1

impact the IBD rate measurement with the same direction and magnitude in all detectors, cancel automatically.

To facilitate comparison between analyses, we note that the analysis presented in this document is performed independently of other θ_{13} analyses and thus constitutes a separate cross-check of all the quantities involved. The only exception are the smaller background contributions. We have independently estimated the largest background source, which are the accidentals, using our own sample of singles. For the remaining smaller background sources however (e.g. ^{9}Li/^{8}He, fast neutrons, etc.), we have used estimates that are based on the extensive studies from other groups.

The note is roughly organized into two main portions. First is a discussion of the ingredients that go into the analysis, such as the IBD selection, the background estimation, and the determination of the various efficiencies that are needed for a relative measurement. A detailed description of the analysis and all of its components follows, which encompasses the rate predictions, the oscillation fit, the assessment of the systematic errors and the results.

2   Dataset

The results presented in this documentation are based on the final P12B datatset (from 24-Dec-2011 to 17-Feb-2012) using the unblinded baselines [2], reactor power and target masses[3]. For readers interested in comparing our previous (blinded) results using the data up to 03-Feb-2012, please refer to documents [4] and [5].

The good run list used in this analysis is obtained from the Data Quality Working Group. The file was downloaded from: `http://neutrino1.physics.sjtu.edu.cn/DQTests/frozen_sets/good_files_3sites_prl_2012-2-21_v1.dat`.

3   IBD Candidate Selection

3.1   IBD Selection

To select IBD candidates, we apply the same cuts as used by the BCW group [6]. IBD events are characterized by the coincidence of an energy deposition by positrons followed by a neutron capture signal by Gadolinium. Once neutrons are captured by Gadolinium with a mean lifetime of ~ 28 μsec, photons with a total energy of about 8.05 MeV are emitted, resulting in a signal that is clearly distinguishable from radioactive backgrounds. The following cuts are applied to select IBD events.

3.1.1   Timing cut

The first step of the IBD selection is to find a set of events with small time separation. Figure 1 shows the observed timing separation of the prompt and delayed signals of the IBD candidates in EH1-AD1. To ensure that we select most of the IBD events and eliminate accidental backgrounds, we require the time separation between the prompt and the delayed signal (Δt) to be:

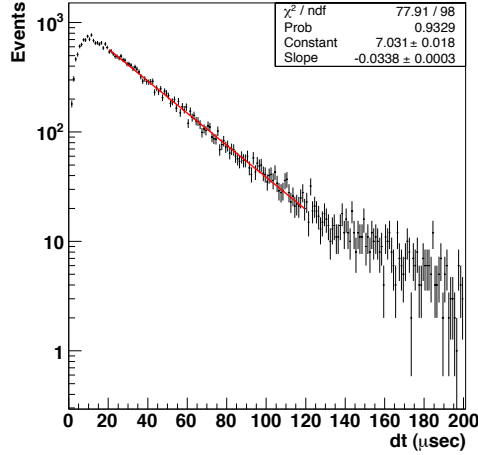$$1 < \Delta t < 200 \ (\mu\text{sec.}).$$

Figure 1: Timing separation of the prompt and delayed signal of the IBD candidates in EH1-AD1.

3.1.2 Energy cut

The deposited energies are reconstructed by using the AdSimple reconstruction package. The details of this algorithm are described in [7] and [8]. For each selected prompt and delayed pair, we require that the corresponding reconstructed energies ($E_{prompt}, E_{delayed}$) to be:

- $0.7 < E_{prompt} < 12.0$ (MeV), and

- $6.0 < E_{delayed} < 12.0$ (MeV).

Figure 2 shows a distribution of the prompt vs. delayed energy distribution of IBD candidates in EH1-AD1. We can clearly see a cluster of IBD events in this energy region. The positron signals are associated by two annihilation photons with total energy of 1.022 MeV in addition to ionization energy loss by positrons. Therefore, the cut at 0.7 MeV for prompt signal is well below the energy threshold expect for IBD events. The efficiency for the prompt signal is nearly 100% and have negligible uncertainty. The cut at 6.0 MeV for delayed signal, however, have inefficiency of ∼10% due to leakage of photons emitted by Gd-capture. Energy scale shifts and other AD response uncertainty can vary the efficiency of this 6-MeV cut, which makes this cut to be one of the dominant systematic uncertainties for the IBD selection. The detail of this systematic uncertainty will be discussed in later sections.

3.1.3 Flasher cut

Before applying any cuts, so called "flasher" events, which caused by a light produced by PMT itself, are the dominating events near the 8-MeV Gd-capture region. Those flusher events formed large number of accidental backgrounds. However, those events have following peculiar PMT hit pattern which enables us to discriminate those events from physics events:

- Very high charge observed in the flashing PMTs.

- Flashing light is collimated and produce more hits in PMTs in opposite side than neighbors.

- PMT hit time distributions is broad as time propagates from one side of the AD to the other.
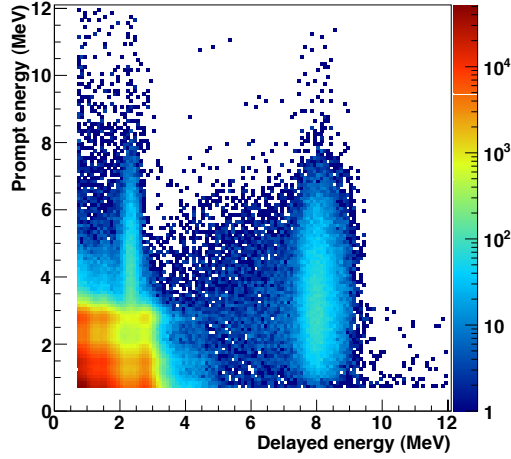
Figure 2: Prompt vs. delayed energy distribution of the IBD candidates in EH1-AD1.

The following cuts are applied to remove flasher events:

- $Quadrant^2 + (MaxQ/0.45)^2 < 1$

- Time PSD cut

- 2" PMT flasher cut

Note that this flasher cut is applied before applying the multiplicity cut described below. More details of the flasher cuts can be found elsewhere.[9, 10]

3.1.4 Muon veto

To eliminate backgrounds from spallation products of cosmic muons, a muon veto is applied. The following criteria are used when tagging an event as a muon:

- AD Muon: the total charge (nominal charge) collected by an AD exceeds 3000 p.e.,

- AD Shower Muon: the total charge collected by an AD exceeds 3×10^5 p.e.,

- Water Pool Muon: the number of PMT hits in inner water system (IWS) or outer water system (OWS) is greater than 12 hits.

An AD is vetoed $1400\,\mu s$ after an AD muon tagged by itself, while all ADs at the same site are vetoed $600\,\mu s$ after a water pool muon. An additional 0.4 s after AD shower muon is added to further reduce backgrounds from spallation ^{8}He/^{9}Li. Cross triggers, with trigger word 0x10000002, of water pool system are not counted as a water pool muon. Cross trigger is issued occasionally by an AD trigger, forcing the water pool system to be read out. It results in a large number of PMT hits in the water pool system, and causes a fake muon signal. Due to the latency between AD and water pool system trigger electronics, an $2\,\mu s$-veto before any muon is introduced. Table 1 summarizes all the types of muon veto cuts applied in this note, which are the same as for the BCW analysis.

Table 1: Summary of Muon Veto Cuts

Type	Cut	Veto w.r.t. Muon Time
AD Muon	Nominal Charge > 3000 p.e.	(-2 μs, 1400 μs)
AD Shower Muon	Nominal Charge > 3×10^5 p.e.	(-2 μs, 0.4004 s)
IWS Muon	nHit > 12	(-2 μs, 600 μs)
OWS Muon	nHit > 12	(-2 μs, 600 μs)

3.1.5 Multiplicity cut

Finally, to prevent accidental hits to distort the observed energy spectrum, we apply so called the "Decoupled Multiplicity Cut" (DMC). In the DMC, we require:

- Only one prompt candidate within 200 μsec before the delayed candidate.

- No other prompt candidate within 400 μsec before the delayed candidate.

- No other delayed candidate within 200 μsec after the delayed candidate.

The details of the DMC studies are described in [6].

3.2 Selected IBD events

Figure 3 shows the vertex distributions for the prompt and delayed events in the IBD candidates. We confirm that the reconstructed vertexes are uniformly distributed within the Gd-LS region.

The distributions of the observed prompt and delayed energy for all six ADs are shown in Fig. 4.

Table 2: Number of observed IBD candidates.

AD1	AD2	AD3	AD4	AD5	AD6
28716	28878	22180	3536	3464	3461

Table 2 summarizes the number of IBD candidate we found in the dataset. The observed number of events in each day is shown in Fig. 5.
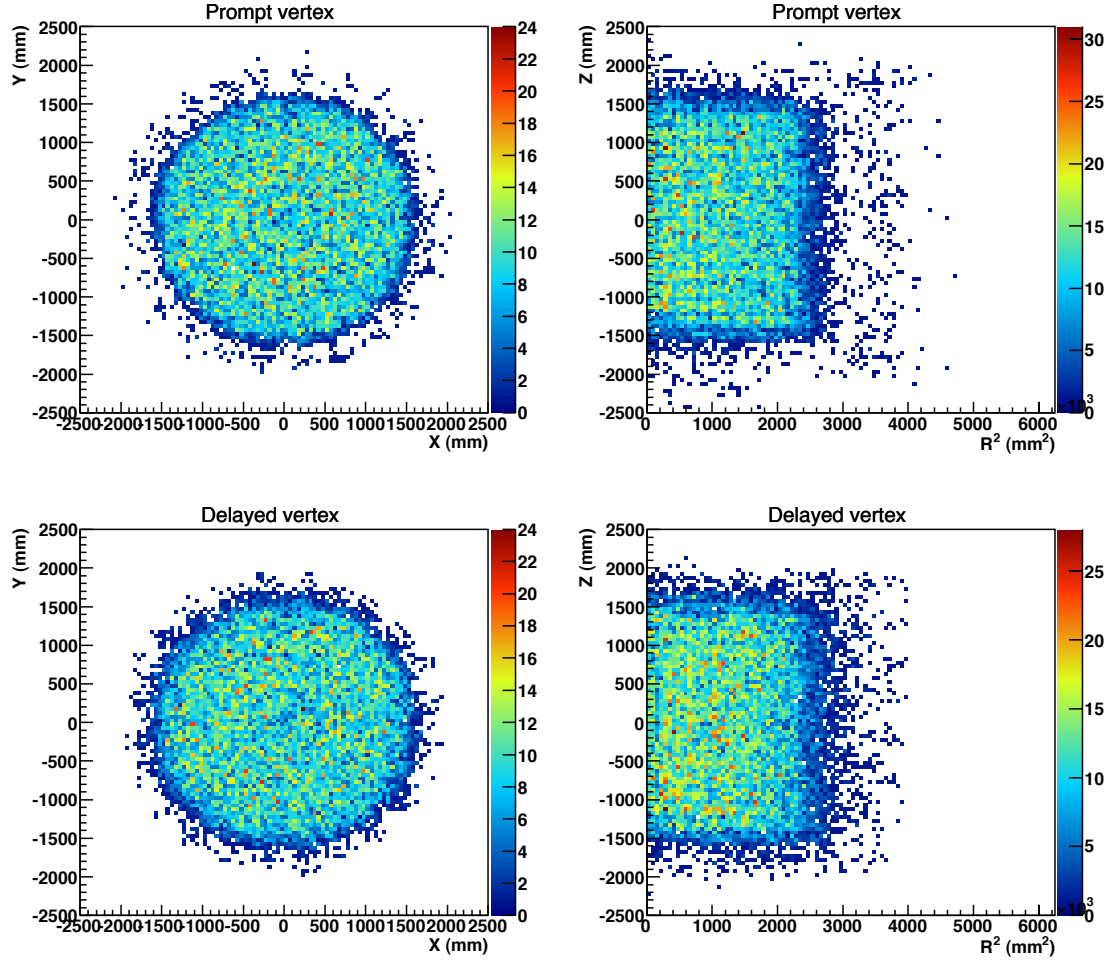
Figure 3: Distributions of reconstructed vertexes for the prompt events (top) and the delayed events (bottom) for the IBD candidates in EH1-AD1.
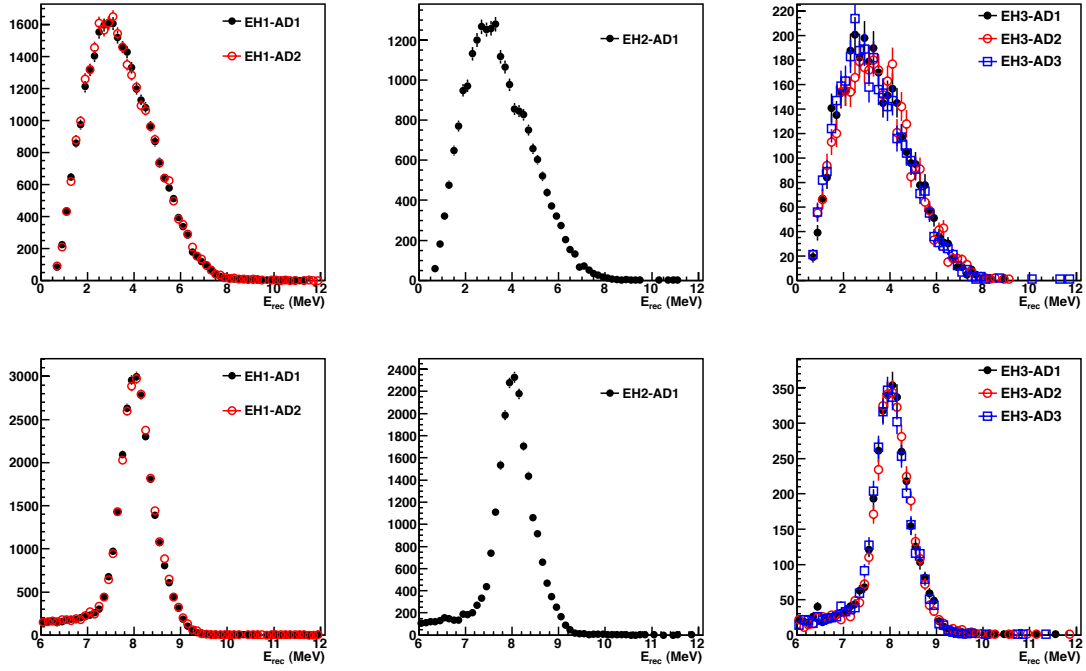
Figure 4: Distributions of reconstructed energy for the prompt events (top) and the delayed events (bottom) for the IBD candidates for all six ADs.
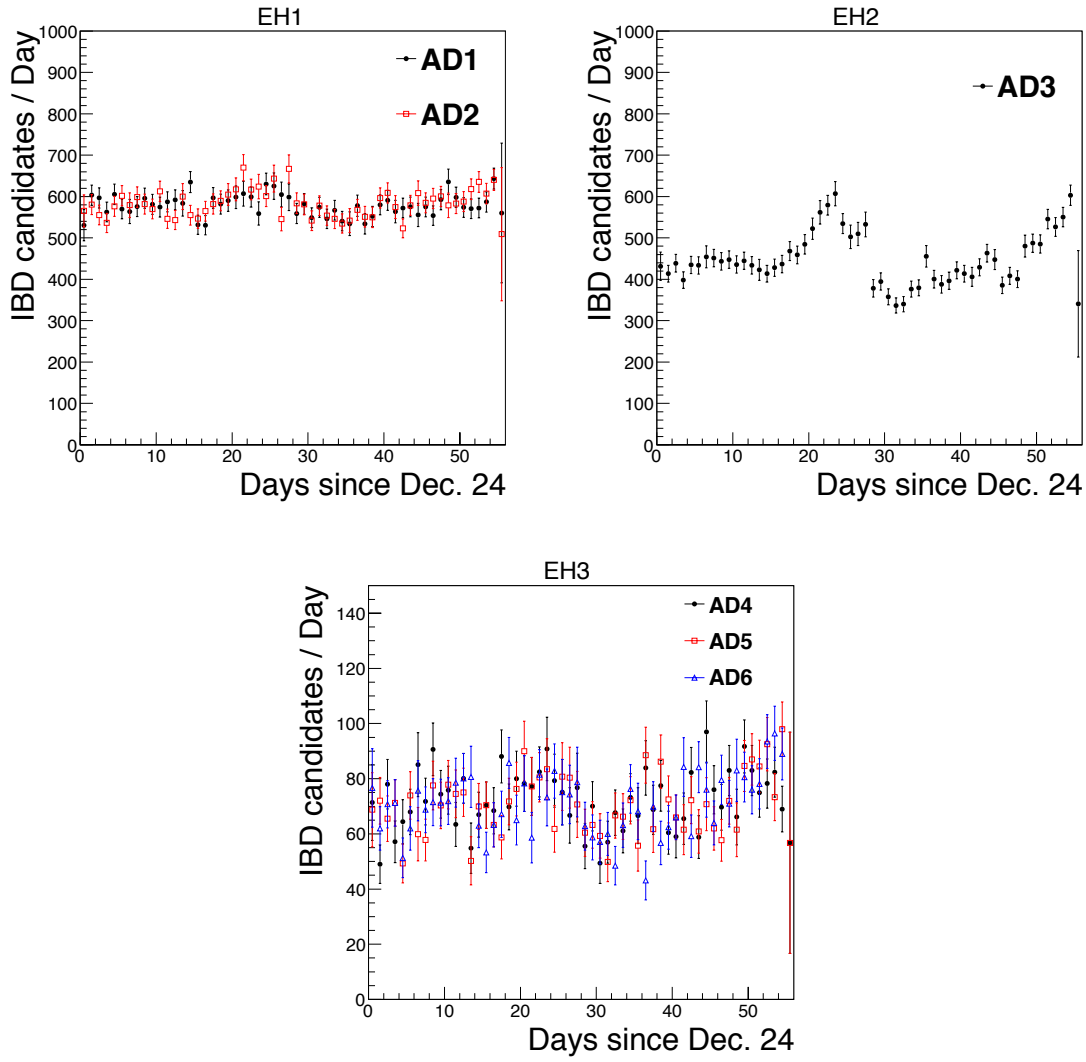
Figure 5: Observed number of IBD candidates in each day at EH1 (top left), EH2 (top right) and EH3 (bottom). Backgrounds are not subtracted. No efficiency corrections are made for this plot.

4 Efficiency Corrections

4.1 Muon Veto Efficiency

In order to reduce fake antineutrino signals from muon-induced radioactivity of the detector, data followed by muon events is vetoed. The corresponding cuts were summarized in Section 3.1.4.

The muon veto time is counted as deadtime of the detector, and subtracted from the raw DAQ livetime. The signal efficiency of the muon veto cut (ϵ_μ) is defined as the muon veto subtracted livetime divided by raw DAQ livetime. If two or more muon veto time windows overlap, they are merged to a single veto time window to avoid double counting. Figure 6 shows the daily signal efficiency of muon veto cut for each ADs.
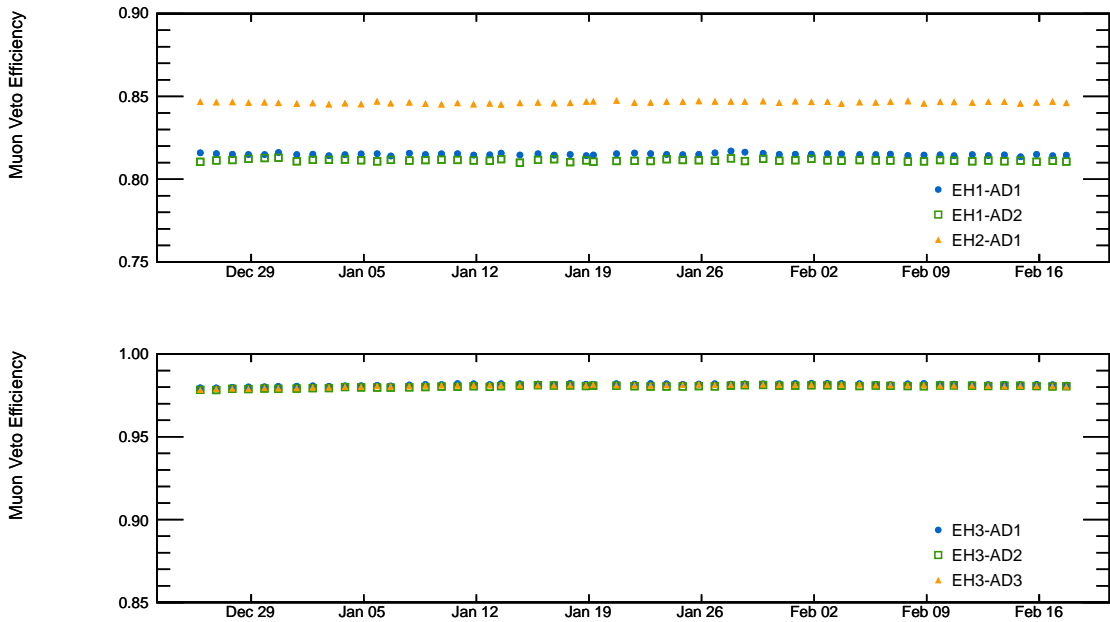

Figure 6: Daily signal efficiency of muon veto cut from Dec 24, 2011 to Jan 17, 2012.

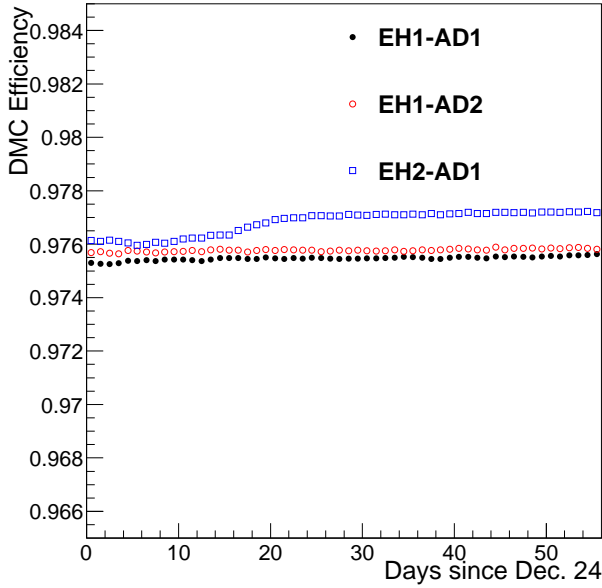## 4.2 Multiplicity Cut Efficiency

A real IBD event gives exactly a pair of prompt-delayed readouts, which are produced by positron and neutron capture. However, a background-like event may be mixed with an IBD event accidentally, thus causing ambiguity in the grouping of prompt-delay pairs. Decoupled multiplicity cut [11] is introduced to ensure only one prompt-delayed pair is formed for IBD candidates. The DMC is applied for every prompt-delay pair by requiring:

- only one prompt candidate within 200 μs before the delayed candidate;

- no prompt candidate in the 200 μs- 400 μs window before the delayed candidate;

- after the prompt-delay pair, no other delayed candidate within 200 μs, or before next muon, whatever comes first.

9

The efficiency on DMC is calculated by $p(0; R_p \times 400\,\mu\text{s}) \times p(0; R_d \times 200\,\mu\text{s})$, where $p(k; \lambda) = \lambda^k e^{-\lambda}/k!$ is the Poisson distribution with expected (λ) and observed (k) number of events, and R_p, R_d are the single rates of prompt-like and delayed like events respectively (Table 3). Detail of single rate calculation is discussed in the following section. The daily signal efficiencies of DMC for six ADs are shown in Fig.7.

Table 3: Summary of Single Rate

Detector	R_p(Hz)	R_d(Hz)
EH1-AD1	62.1527	0.00933302
EH1-AD2	61.3592	0.00954638
EH2-AD1	58.7428	0.00765279
EH3-AD1	65.0247	0.00298085
EH3-AD2	66.0320	0.00298560
EH3-AD6	66.3200	0.00278266
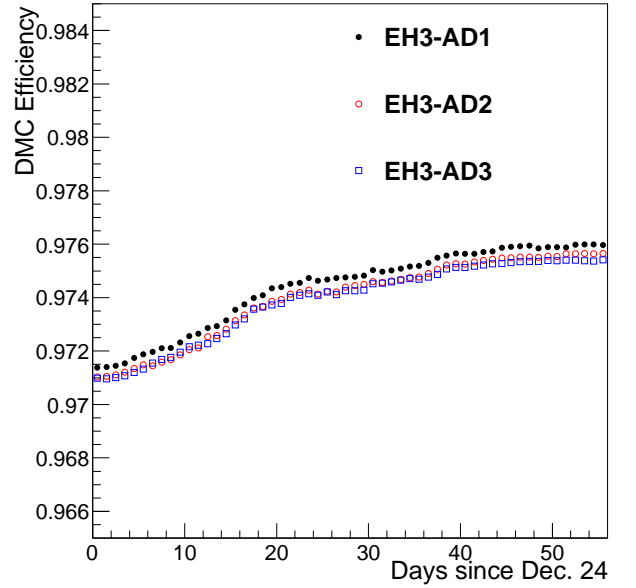
(a) Near sites   (b) Far site

Figure 7: Signal efficiency of decoupled multiplicity cut since Dec 24, 2011.

5 Backgrounds

5.1 Accidentals

Accidental backgrounds are estimated using singles rate observed in the data. Those singles event must pass the IBD selection criteria, except for the requirement for the prompt-delayed pair within

199 μsec separation. Then, accidental coincidence of such singles events form the accidental backgrounds.

The cuts applied to select singles rate is the followings:

- Muon veto cut, with the same condition as applied to IBD candidates.

- Flasher cut, with the same condition as applied to IBD candidates.

- DMC cut, except for requirements for the one prompt signal. i.e. no prompt-like signal within 400 μ sec before and no delayed-like signal within 200 μ sec after the event.

The spectrum of the singles events after applying those cuts are shown in Fig. 8. Before applying the DMC cut, the large fraction of the events in the delayed energy region ($6.0 < E_{rec} < 12.0$ MeV) are neutrons from IBDs. Those IBD events are removed by applying the DMC cut. Then, we obtain the "pure" singles rate which passes the all IBD selection cuts but does not form correlated prompt-delayed pair.
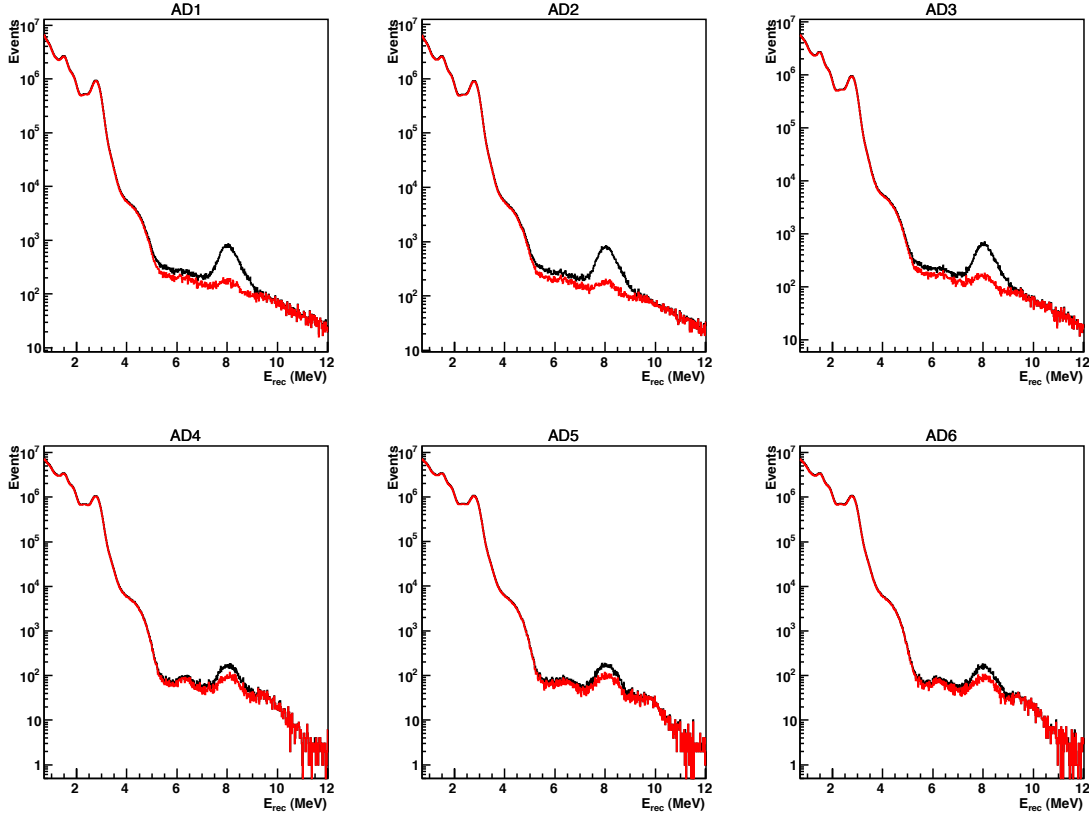

Figure 8: Spectrum of the singles events for all 6 ADs. The black curves show the distribution after applying muon veto and flasher cuts, but before applying the DMC cut. The red curves show the distribution after all cuts.

We estimate the number of accidental backgrounds by following the method described in [12] by Xin and Fenfang. We define the observed rate of singles events in prompt and delayed energy regions as R_p^{single} and R_d^{single}, respectively. To calculate the accidental rate, we need to correct

muon veto and multiplicity cut efficiency. The corrected singles rate, $R_p^{single,corr}$ and $R_d^{single,corr}$, are calculate as:

$$R_p^{single,corr} = R_p^{single}/P(0, R_p^{all} \times 400\mu sec)/P(0, R_d^{all} \times 200\mu sec)/\epsilon_\mu \qquad (1)$$

$$R_d^{single,corr} = R_d^{single}/P(0, R_p^{all} \times 400\mu sec)/P(0, R_d^{all} \times 200\mu sec)/\epsilon_\mu, \qquad (2)$$

where R_p^{all} and R_d^{all} are event rate in prompt and delayed energy regions before applying the DMC cut, $P(0, \nu)$ is the Poisson probability of finding 0 event when the expected value is ν, and ϵ_μ is the muon veto efficiency. Then, accidental event rate, R^{acci}, is calculated as:

$$R^{acci} = 199\mu sec \times R_p^{single,corr} \times R_d^{single,corr}. \qquad (3)$$

The estimated rate of the accidental backgrounds for each day is shown in Fig. 9. The estimated accidental background rate for the entire dataset is summarized in Tab. 4.
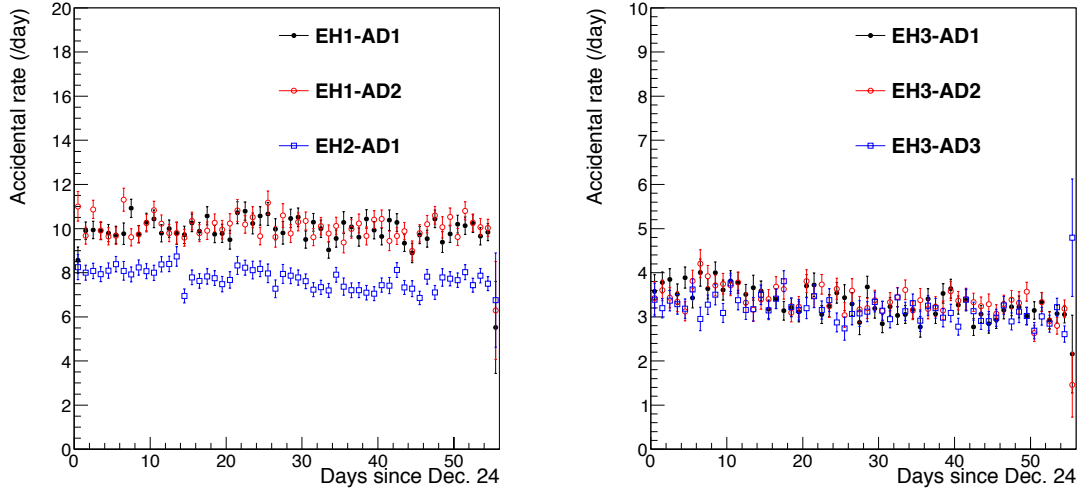

Figure 9: Estimated rate of the accidental backgrounds in EH1 and EH2 (left), and in EH3 (right); The muon veto and multiplicity cut efficiency are corrected.

Table 4: Summary of accidental backgrounds for the entire dataset (events/live-day).

AD1	AD2	AD3	AD4	AD5	AD6
9.97 ± 0.056	10.07 ± 0.056	7.73 ± 0.047	3.34 ± 0.030	3.39 ± 0.031	3.17 ± 0.030

5.2 ^{8}He/^{9}Li and Fast Neutrons

Besides accidental background, ^{8}He/^{9}Li from muon spallation are one of the major source of background. The β-decay of ^{9}Li ($\tau_{1/2} = 178.3$ ms, $\Delta Q = 13.61$ MeV) and ^{8}He ($\tau_{1/2} = 119.0$ ms, $\Delta Q = 10.65$ MeV) sometimes produce a neutron unstable daughter states, which mimicks the prompt-delayed IBD signal. The lifetime of these isotopes are relatively long after muon spallation, which

cannot be removed completely by muon veto cut. Several studies [13], [14], and [15] have been done to estimate the rate of ^{8}He/^{9}Li backgrounds by fitting the time since muon of the delayed-like events.

Fast neutrons are neutrons produced by untagged muons, or energetic neutrons produced outside the muon system passing through the detector. Suppose all fast neutrons have a flat prompt energy distribution, the background rate can be calculated by extrapolating from high energy ($> 12~MeV$) region to the IBD signal region. Table 5 and 6 list background rate used in this note for ^{8}He/^{9}Li and fast neutrons at each site.

Table 5: Summary of ^{8}He/^{9}Li background rate after muon veto cut [15].

Site	Rate (/AD/live-day)
EH1	$2.74 \pm 0.20 \pm 0.61$
EH2	$1.45 \pm 0.16 \pm 0.88$
EH3	$0.16 \pm 0.06 \pm 0.06$

Table 6: Summary of fast neutrons background for each site [16].

Site	Rate (/AD/live-day)
EH1	$0.95 \pm 0.04 \pm 0.28$
EH2	$0.71 \pm 0.06 \pm 0.21$
EH3	$0.07 \pm 0.01 \pm 0.02$

5.3 ^{241}Am^{13}C and ^{13}C$(\alpha, \mathrm{n})^{16}$O

The calibration source ^{241}Am^{13}C stored on the top of AD produces a single neutron at a rate of 0.5 Hz. Inelastic scattering of the neutron with nuclei in the stainless steel gives a prompt gamma signal. The neutron is then captured by nuclei in the stainless steel, and releases another delayed gamma signal. A small fraction of these correlated high energy gammas can enter the AD, and causes an IBD-like background event. The background rate of ^{241}Am^{13}C is estimated from data [17] and simulation [18]: 0.2 ± 0.2 events per day per AD.

The background rate of ^{13}C$(\alpha, \mathrm{n})^{16}$O is measured from alpha rate integrated with ^{13}C$(\alpha, \mathrm{n})^{16}$O cross section (Table 7).

Table 7: Summary of ^{13}C$(\alpha, \mathrm{n})^{16}$O background [19].

Site	Rate (/AD/live-day)
EH1	0.05 ± 0.02
EH2	0.045 ± 0.02
EH3	0.04 ± 0.02

U^{235}	U^{238}	Pu^{239}	Pu^{241}
0.64	0.08	0.25	0.03

Table 8: Nominal isotope fractions used to generate the nominal anti-neutrino energy spectrum in the Daya Bay ADs for the blind analysis.

6 Predicting the far AD rates

6.1 Oscillation Probability

Even for a rate analysis, it is necessary to take into account the spectral shape of the prompt IBD events in order to calculate the oscillation probability. The $\bar{\nu}_e$ energy spectrum of U^{235}, Pu^{239}, Pu^{241} were experimentally determined by the ILL High-Flux Reactor in Grenoble, France [21, 22] while the U^{238} spectra is calculated theoretically [23]. The ILL spectra are interpolated as described in [20]. The inverse beta decay cross section as given in Ref.citeVogelAnuSpectra is recalculated with updated PDG constants such as phase factor f^R=1.71465, axial-vector coupling g_A=1.2701, and neutron lifetime=881.5 seconds[1]. A detailed description of the cross section can be found in [25]. Figure 10 shows the raw isotope spectra and IBD cross section used in our analysis.
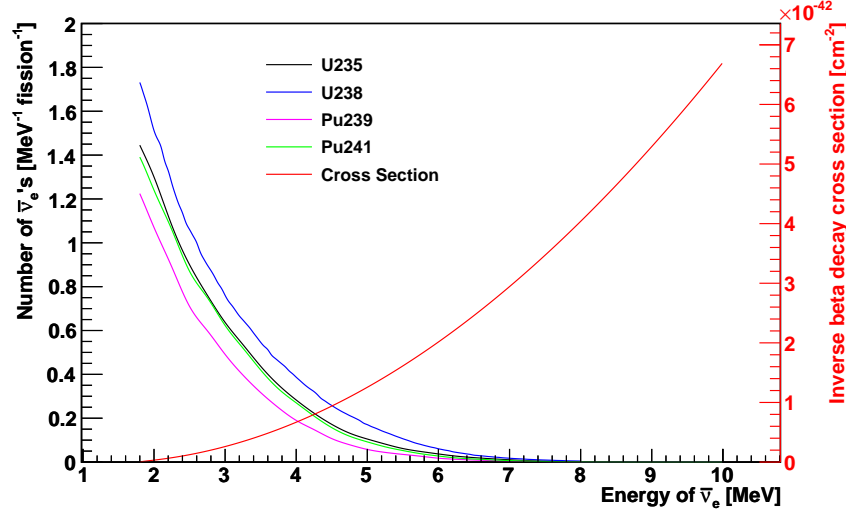

Figure 10: The $\bar{\nu}_e$ energy spectrum from different fission isotope U^{235}, U^{238}, Pu^{239}, Pu^{241}. The inverse beta decay cross section as a function of $\bar{\nu}_e$ energy is shown in red line.

To obtain the true energy spectrum of anti-neutrinos, we need to know the fission fractions of each isotope and the power output in the different Daya Bay and Ling Ao cores. These are provided by the Nuclear Power Plant on a weekly basis. During the period when the reactor flux was blinded, the nominal isotope fractions shown in Table 8 were used to generate the spectrum for the blind analysis.

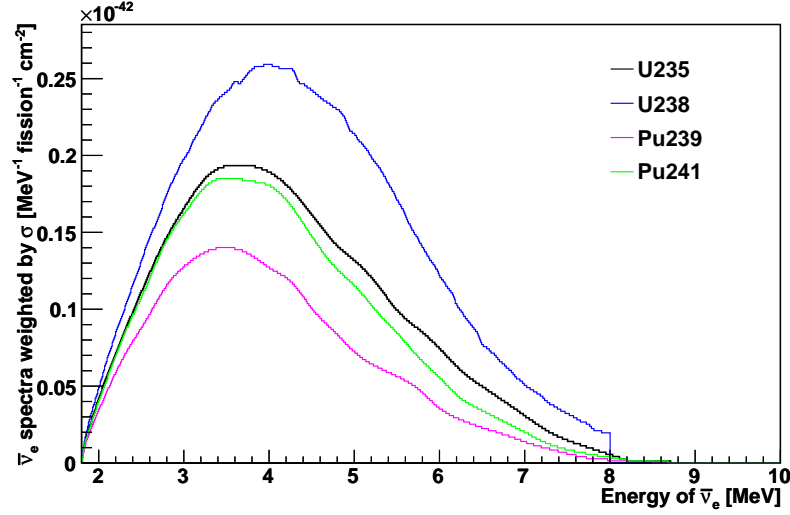[1]We thank Dan Dwyer, Wei Wang for tabulating those data

Figure 11: The $\overline{\nu}_e$ energy spectrum of different fission isotope U^{235}, U^{238}, Pu^{239}, Pu^{241} weighted by the inverse beta decay cross section.

Figure 11 shows the true energy spectra of anti-neutrinos produced in the fissions of the different core isotopes per fission. They are obtained by taking the product of the raw anti-neutrino spectra with the IBD cross-section, as defined above. The four spectra are quite similar, although they differ in amplitude and peak position. Their linear combination in the proportions of Table 8 gives the spectra that is used to generate the oscillation probability (left of Figure 13). That spectrum is more coarsely rebinned in order to reduce the computation time.

We use the full expression for electron anti-neutrino disappearance, as given by the following equation:

$$
\begin{aligned}
\mathrm{P}(\overline{\nu_e} \to \overline{\nu_x}) \;=\; & \cos^2(\theta_{12}) \sin^2(2\theta_{13}) \sin^2\left(\frac{\Delta m_{31}^2 L}{4E}\right) \\
+ \; & \sin^2(\theta_{12}) \sin^2(2\theta_{13}) \sin^2\left(\frac{\Delta m_{32}^2 L}{4E}\right) \\
+ \; & \sin^2(2\theta_{12}) \cos^4(\theta_{13}) \sin^2\left(\frac{\Delta m_{21}^2 L}{4E}\right)
\end{aligned}
\tag{4}
$$

The survival probability is plotted as a function of baseline in Figure 12 under different assumptions. The "one term" case corresponds to when only the dominant term is kept in the expression of the probability (i.e. $\sin^2(2\theta_{13}) \sin^2\left(\frac{\Delta m_{32}^2 L}{4E}\right)$), and it seems to be not good enough for our purposes. The "two-term" case is reached under the assumption that $\Delta m_{31}^2 \sim \Delta m_{32}^2$, which results in the reduction of Equation 4 to two terms. The last case is the one that we follow and which allows us to properly distinguish the normal and inverted neutrino mass hierarchy scenarios.

The results shown in the rest of this note are obtained by evaluating Equation 4 using the values that the Particle Data Group reported in 2011. It is then applied to the true energy spectra of anti-neutrinos and the ratio of the integrals of the oscillated to the unoscillated spectra is computed. The result as a function of distance L is shown on the right of Figure 13. For simplicity, all plots shown are obtained under the assumption of the normal hierarchy (namely,
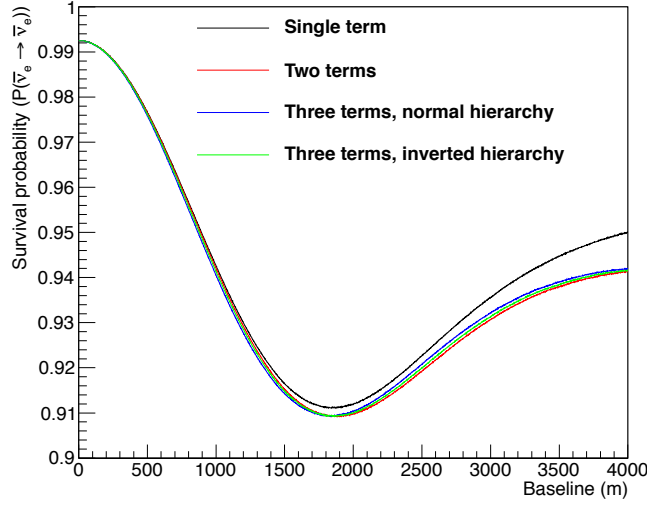
Figure 12: Survival probability of anti-neutrinos as a function of baseline, for a fixed $\sin^2(2\theta_{13})$ of 0.1, when only certain terms are kept in the calculation.

$\Delta m^2_{31} = \Delta m^2_{32} + \Delta m^2_{21} \sim 2.51 \times 10^{-3}\text{eV}^2$). The shift that is introduced in the best fit $\sin^2(2\theta_{13})$ by considering the inverted hierarchy is analyzed in the results section.
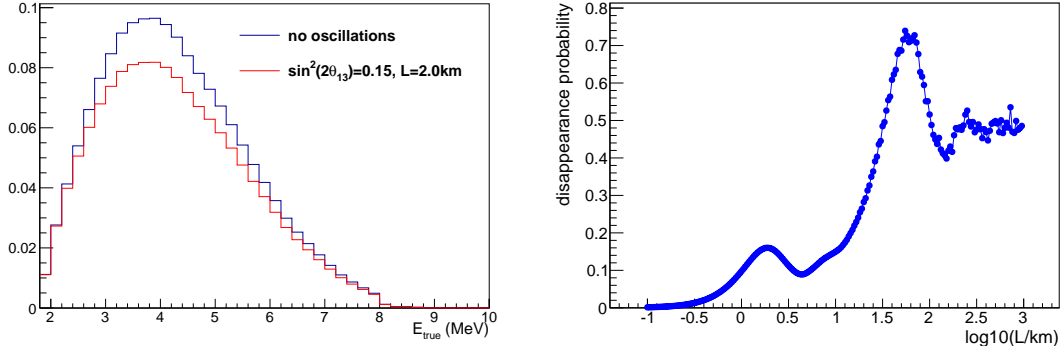
Figure 13: Anti-neutrino disappearance probability (right) obtained by weighing the true energy spectrum (left) by Equation 4 and taking the ratio of the integrals.

6.2 Flux Matrices

6.2.1 General Concept

We use the unblinded coordinates of the ADs and the reactor cores[2], which result in the baselines laid out in Table 9. From the baselines and the knowledge about the relative power of the reactor cores it is possible to construct a so-called "flux matrix." Each element f_{ij} in this matrix corresponds to the percentage of the total IBD rate observed in AD i due to core j and, under the assumption

16

	D1	D2	L1	L2	L3	L4
AD1	362.377	371.759	903.471	817.162	1353.622	1265.319
AD2	357.937	368.411	903.351	816.900	1354.234	1265.890
AD3	1332.475	1358.144	467.571	489.574	557.580	499.207
AD4	1919.629	1894.335	1533.178	1533.625	1551.382	1524.937
AD5	1917.517	1891.975	1534.917	1535.030	1554.765	1528.043
AD6	1925.255	1899.861	1538.929	1539.467	1556.342	1530.076

Table 9: Baselines between the six ADs and the six reactor cores as obtained from the unblinded coordinates, in meters.

	D1	D2	L1	L2	L3	L4
AD1	0.4063	0.3860	0.0654	0.0799	0.0291	0.0333
AD2	0.4094	0.3864	0.0643	0.0786	0.0286	0.0327
AD3	0.0330	0.0317	0.2678	0.2443	0.1883	0.2349
AD4	0.1208	0.1241	0.1894	0.1893	0.1850	0.1915
AD5	0.1213	0.1246	0.1893	0.1893	0.1845	0.1910
AD6	0.1209	0.1242	0.1893	0.1891	0.1850	0.1915

Table 10: Flux matrix obtained assuming no oscillations and equal power on all reactor cores.

of equal fission fractions for all cores, is calculated in the following way:

$$f_{ij} = \frac{\frac{P_j \times P_{ij}^{\mathrm{osc}}}{r_{ij}^2}}{\sum_j \frac{P_j \times P_{ij}^{\mathrm{osc}}}{r_{ij}^2}}, \tag{5}$$

where P_j is the power of core j, P_{ij}^{osc} is the disappearance probability of anti-neutrinos traveling from core j to AD i, and r_{ij} is the corresponding baseline. Each row of the flux matrix is normalized so that the total is 1. In the case of no oscillations and equal power for all cores, the matrix calculation depends uniquely on the baselines and reduces to what is shown in Table 10. As expected, the near site ADs sample a much less balanced flux compared to the Far site ADs. Specifically, the Far ADs see a roughly equal contribution of $12 - 18\%$ from each core, while the near site ADs see 80% of their events from either the Daya Bay or the Ling Ao cores.

As shown in the next section, only the first three rows (those that correspond to the near ADs) are used in the prediction of the far AD rates. For them, the impact of oscillations is small, as illustrated in the example shown in Table 11. As expected, when oscillations are accounted for, the ADs see an increased contribution from the reactor cores that are closer to them, although it is a very small effect.

6.2.2 Handling the Time Dependence

When considering periods of time with varying reactor flux and with reactors at different stages of their fuel cycles, the construction of the flux matrix becomes slightly more complicated. Nonethe-

17

	D1	D2	L1	L2
AD1	0.410	0.389	0.063	0.078
AD3	0.031	0.030	0.269	0.245

Table 11:   A subset of the flux matrix shown in Table 10 but with $\sin^2(2\theta_{13}) = 0.10$.

	D1	D2	L1	L2	L3	L4
AD1	0.417	0.427	0.039	0.054	0.030	0.034
AD2	0.419	0.427	0.038	0.053	0.029	0.033
AD3	0.041	0.042	0.193	0.201	0.235	0.288
AD4	0.140	0.154	0.127	0.145	0.215	0.219
AD5	0.140	0.155	0.126	0.145	0.215	0.218
AD6	0.140	0.154	0.127	0.144	0.215	0.219

Table 12:   Flux matrix obtained for the period of Dec. 24 to Feb. 17, based on the unblinded reactor data, for $\theta_{13} = 0$.

less, it is still possible to encapsulate the knowledge of the flux into one single matrix. This can be achieved by weighing the flux Φ_{ij}^{τ} seen in each AD i from each core j at a given time bin τ, by the livetime L_i^{τ} and the efficiency ϵ_i^{τ} of that given AD

$$
f_{ij} = \frac{\sum_{\tau} \phi_{ij}^{\tau} \times L_i^{\tau} \times \epsilon_i^{\tau} \times P_{ij}^{\text{osc}}}{\sum_{j} \sum_{\tau} \phi_{ij}^{\tau} \times L_i^{\tau} \times \epsilon_i^{\tau} \times P_{ij}^{\text{osc}}},
\tag{6}
$$

where, once again, the matrix is normalized in such a way that the sum of the elements of each row equals 1. The efficiencies ϵ_i^{τ} are the product of the muon veto efficiencies and the DMC efficiencies. The flux Φ_{ij}^{τ} is calculated by taking into account the relative fission fractions of each isotope at time τ, the relative fission rate at time τ, and is inversely proportional to the square of the baseline r_{ij}. The fission rate at each core can be calculated from the overall power output divided by the average energy produced per fission, which is just a sum of the average energy released per fission for each isotope weighted by the isotope fission fraction.

For the period of Dec. 24 to Feb. 17, the flux matrix that is obtained using the unblinded reactor data is shown in Table 12. A comparison with the one in Table 10 reveals that, as expected, the relative contributions of the L1 and L2 cores on all ADs are diminished, given the fact that both of these cores were off for a significant amount of time during the period considered.

This method of encapsulating all of the reactor knowledge into a single matrix (Method A) is preferred, due to its simplicity. To the degree that the detector efficiencies and dead times are roughly constant in time, the method should not introduce any biases. In order to quantify any error arising from this procedure, an alternative way (Method B) of predicting the far AD rates was also explored. Such a method consists in treating the eight periods of time in which we have unblinded reactor data available separately, each with its number of IBD events and detector efficiencies, and then summing all the contributions.

	D1	D2	L1	L2	L3	L4
From 2011-12-24 00:00:00 to 2011-12-31 00:00:00						
AD1	0.426	0.438	0.068	0.0	0.032	0.036
AD2	0.429	0.438	0.067	0.0	0.031	0.035
AD3	0.043	0.045	0.344	0.0	0.253	0.315
From 2011-12-31 00:00:00 to 2012-01-07 00:00:00						
AD1	0.426	0.438	0.068	0.0	0.032	0.036
AD2	0.429	0.438	0.067	0.0	0.031	0.035
AD3	0.043	0.045	0.344	0.0	0.253	0.315
From 2012-01-07 00:00:00 to 2012-01-14 00:00:00						
AD1	0.417	0.428	0.066	0.021	0.031	0.035
AD2	0.420	0.428	0.065	0.021	0.030	0.034
AD3	0.040	0.041	0.318	0.077	0.234	0.290
From 2012-01-14 00:00:00 to 2012-01-21 00:00:00						
AD1	0.396	0.406	0.061	0.079	0.029	0.029
AD2	0.399	0.406	0.059	0.079	0.028	0.029
AD3	0.034	0.035	0.262	0.026	0.196	0.218
From 2012-01-21 00:00:00 to 2012-01-28 00:00:00						
AD1	0.428	0.438	0.0	0.079	0.026	0.029
AD2	0.430	0.438	0.0	0.077	0.026	0.029
AD3	0.050	0.052	0.0	0.035	0.247	0.301
From 2012-01-28 00:00:00 to 2012-02-04 00:00:00						
AD1	0.419	0.427	0.0	0.087	0.031	0.035
AD2	0.422	0.427	0.0	0.086	0.030	0.034
AD3	0.043	0.045	0.0	0.342	0.255	0.315
From 2012-02-04 00:00:00 to 2012-02-11 00:00:00						
AD1	0.418	0.427	0.02	0.087	0.031	0.035
AD2	0.421	0.427	0.01	0.086	0.030	0.034
AD3	0.043	0.045	0.08	0.338	0.253	0.313
From 2012-02-11 00:00:00 to 2012-02-17 00:00:00						
AD1	0.398	0.406	0.050	0.083	0.029	0.033
AD2	0.401	0.407	0.049	0.082	0.029	0.033
AD3	0.034	0.035	0.215	0.268	0.200	0.248

Table 13: Individual flux matrices obtained for the period of Dec. 24 to Feb. 17 divided into eight periods of time, based on the unblinded reactor data, for $\theta_{13} = 0$.

	AD4			AD5			AD6		
Expected from	AD1	AD2	AD3	AD1	AD2	AD3	AD1	AD2	AD3
Method A	75.86	75.14	75.15	75.73	75.01	75.02	75.36	74.64	74.65
Method B	75.84	75.15	75.12	75.71	75.02	74.99	75.34	74.65	74.62

Table 14: Predicted number of events in each of the far ADs, in the case of no-oscillations, for Method A and Method B. All numbers are normalized to one day of livetime and to the target mass of AD1. The differences between the two methods are negligible, being smaller than 0.04%.

Table 13 shows what the time-varying flux matrix looks like for Method B (only for the first three rows, which are the ones used in making the far site predictions). There it can clearly be seen how the L2 core was down for the first two weeks, how it came back up, how L1 powered off shortly after, and how it was powered back up in the last week of the period considered. When calculating the number of expected events in the far ADs (using the methodology described in the next section) with Method B, we find that we get practically the same results than with Method A, as shown in Table 14. In fact, when using Method B to do the fit in $\sin^2(2\theta_{13})$, we see only a difference of 0.1% with method A. Because of this, we choose Method A as our default one, and all of the results shown in the rest of this note are obtained with it.

6.3 Rate Prediction

With the flux matrix it is straightforward to estimate for each AD i the amount of IBD events due to each core j:

$$N_{ij} = f_{ij} \times N_i^{corr} \tag{7}$$

where N_i^{corr} is the observed number of IBD events in AD i after efficiency, muon dead time, and target mass corrections. Each of these components can then be extrapolated separately to a far AD k by correcting for the difference in baselines and the effect of oscillations:

$$F_{kj,i} = N_{ij} \times \frac{L_{ij}^2}{L_{kj}^2} \times \frac{P_{kj}^{\text{osc}}}{P_{ij}^{\text{osc}}}. \tag{8}$$

By summing all the contributions from each core we obtain the total number of IBD events expected in AD k based on AD i

$$F_{k,i} = \sum_j F_{kj,i}, \tag{9}$$

which is thus dependent on θ_{13}. This way, three predictions can be generated for each far AD, each from a near site AD.

It should be noted that this machinery can be applied to generate predictions of any AD based on any other. In other words, it need not be used exclusively to predict the far AD rates based on the near ones but could also, for instance, be used to predict the Ling Ao rate based on the Daya Bay ones. Most of the power to determine θ_{13} however comes from comparing the near and far rates, and thus we do not generate near site predictions for the analysis. Nonetheless, studying the relative near AD predictions is still a useful exercise when it comes to understanding the reactor flux. Table 15 shows the relative rates of the near ADs under different conditions and shows how, for the period of time considered in this analysis, the data agree reasonably well with the hypothesis that one of the Ling Ao cores is off.

	AD1 (ref)	AD2	AD3
All cores on	1	1.017	0.908
D1 off	1	1.012	1.484
D2 off	1	1.017	1.436
L1 off	1	1.018	0.758
L2 off	1	1.019	0.748
L3 off	1	1.018	0.758
L4 off	1	1.018	0.722
data	1	1.01 ± 0.01	0.75 ± 0.01

Table 15: Relative rates in the near ADs (with reference to AD1) under different conditions. The data agree well with one of the Ling Ao cores being down for the period of time that is being considered.

7   Toy Monte Carlo Samples

A toy Monte Carlo was put in place with two different purposes in mind:

- Validating the fitting code for θ_{13} (described in the next section)

- Handling the systematic uncertainties in the analysis

To avoid any biases, the toy Monte Carlo code was developed independently of the θ_{13} fitter. The only shared assumptions during the development were the blinded baselines, the assumptions on the reactor power, and the known PDG values of the oscillation parameters. After the fitter validations were satisfactorily completed, the toy Monte Carlo was expanded to study the various systematic uncertainties and also to properly estimate the statistical significance of the results. Some of the results obtained with the toy MC samples are included in the following sections.

The basic algorithm of the toy Monte Carlo is shown in Figure 14. Given a nominal set of reactor power data, baselines, efficiencies, live time, backgrounds, and a particular value of θ_{13}, a series of toy experiments are generated. The output of each toy experiment is the observed number of events for the six antineutrino detectors. The algorithm fluctuates each input parameter based on the expected uncertainties, with options available to turn each fluctuation on and off independently. The sources of systematic error that are considered are the following:

- Statistical Error: both the statistics in the near and far events are considered, although the ones in the far site dominate.

- Reactor Flux Uncertainties: a 0.8% core-to-core (i.e. uncorrelated) variation is considered.

- Detector Uncertainties: a 0.3% uncorrelated uncertainty is considered. This encapsulates any effects that impact the measured IBD rate from AD to AD, and includes sources such as the uncertainty in the number of target protons and the differences in cut efficiencies. We do not correct for the small time variation in the target masses. However, as estimated in [3], a conservative systematic uncertainty under this assumption is $\sim 0.03\%$. Therefore, the 6MeV cut is by far the dominant source of this systematic error, as estimated in [26] and [27].

- Background Uncertainties: backgrounds are fluctuated by their estimated systematic errors, laid out in Section 5. They are also fluctuated by their statistical error, but under the statistical error rubric mentioned above.

	Reactor Flux	Detector	Backgrounds	Oscillation Parameters
Variation considered	0.8% core-to-core	0.3% uncorrelated	see Tables 4, 5, 6 and 7.	PDG 2011 uncertainties

Table 16: Sources of systematic error and the corresponding variations considered.

- Oscillation Parameter Uncertainties: the various oscillation parameters that go in Equation 4 (with the exception of θ_{13} of course) are also fluctuated by their uncertainties, as given by the PDG.
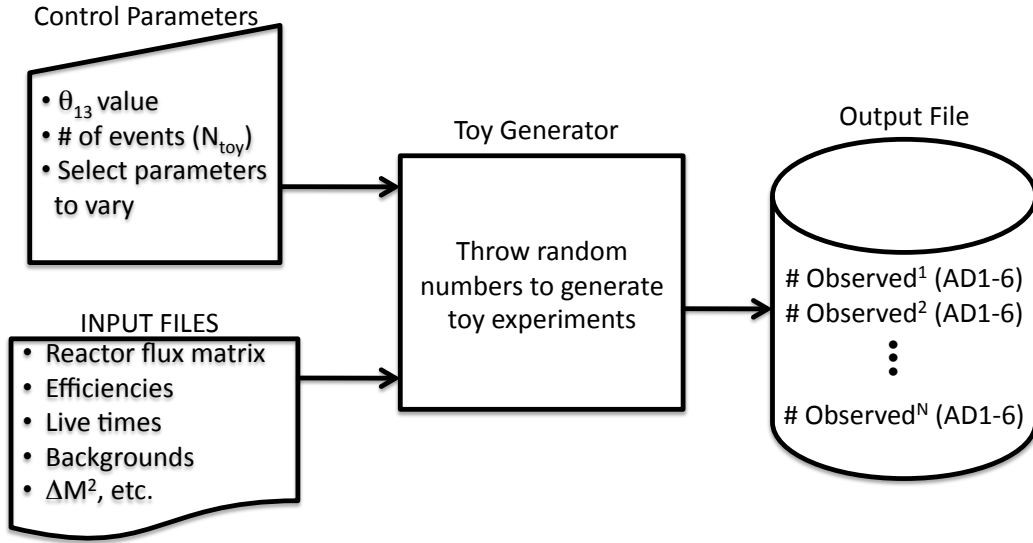

Figure 14: Block Diagram for the toy Monte Carlo.

These sources of systematic error are summarized in Table 16. As previously mentioned, any correlated systematic uncertainties automatically cancel in our measurement, which is why none of them are considered. This includes the correlated power uncertainty in the reactors (typically estimated to be around 3%), as well as the uncertainty in the IBD cross-section, and the absolute IBD detector efficiencies.

8   Oscillation fit

8.1   General Formalism

As previously mentioned, we have a total of nine predictions (three predictions on each far AD from each near AD):

$$\mathcal{F} = \begin{pmatrix} F_{4,1} \\ F_{4,2} \\ F_{4,3} \\ F_{5,1} \\ F_{5,2} \\ F_{5,3} \\ F_{6,1} \\ F_{6,2} \\ F_{6,3} \end{pmatrix} \tag{10}$$

and we can form a χ^2 in the following way:

$$\chi^2 = \sum_{i,j}^{9} (\mathcal{F}_i^{obs} - \mathcal{F}_i^{pred}) V_{ij}^{-1} (\mathcal{F}_j^{obs} - \mathcal{F}_j^{pred}), \tag{11}$$

where V is a 9×9 covariance matrix.

V is constructed by separately considering each source of the uncertainty, as follows:

$$V = V^{stat} + V^{reactor} + V^{eff} + V^{bkg} \tag{12}$$

The elements of the covariance matrices are calculated by using the toy MC sample, as:

$$V_{ij} = \frac{1}{M} \sum^{toys} (\mathcal{F}_i^{obs,toy} - \mathcal{F}_i^{pred,toy})(\mathcal{F}_j^{obs,toy} - \mathcal{F}_j^{pred,toy}), \tag{13}$$

where M is the total number of toy MC events.

It should be noted that the covariance matrix is formed assuming a null oscillation signal (i.e. $\theta_{13} = 0$). In the fit, the matrix is scaled using the ratio of the predicted number of events as a function of θ_{13}:

$$V_{ij}(\sin^2(2\theta_{13})) = V_{ij}(0) \times \frac{F_i^{pred}(\sin^2(2\theta_{13}))}{F_i^{pred}(0)} \times \frac{F_j^{pred}(\sin^2(2\theta_{13}))}{F_i^{pred}(0)} \tag{14}$$

The exception is the matrix for the background systematics and the statistical uncertainty, for which the above scaling is clearly incorrect.[2] The number of backgrounds are not expected to change as a function of θ_{13}. Thus, the matrix for the backgrounds is not scaled at all. That covariance matrix for the statistical uncertainty is analytically calculated by including near-site AD statistics propagated to the far-site expectation, as well as the statistical error for the number of far-site data.

The correlations (quantified as $V_{ij}/\sqrt{V_{ii}V_{jj}}$) for each source are shown in Fig. 15. The correlation for the total systematic and statistical uncertainties are shown in Fig. 16.

---

[2]This was actually corroborated through the use of the Feldman-Cousins method, described later.
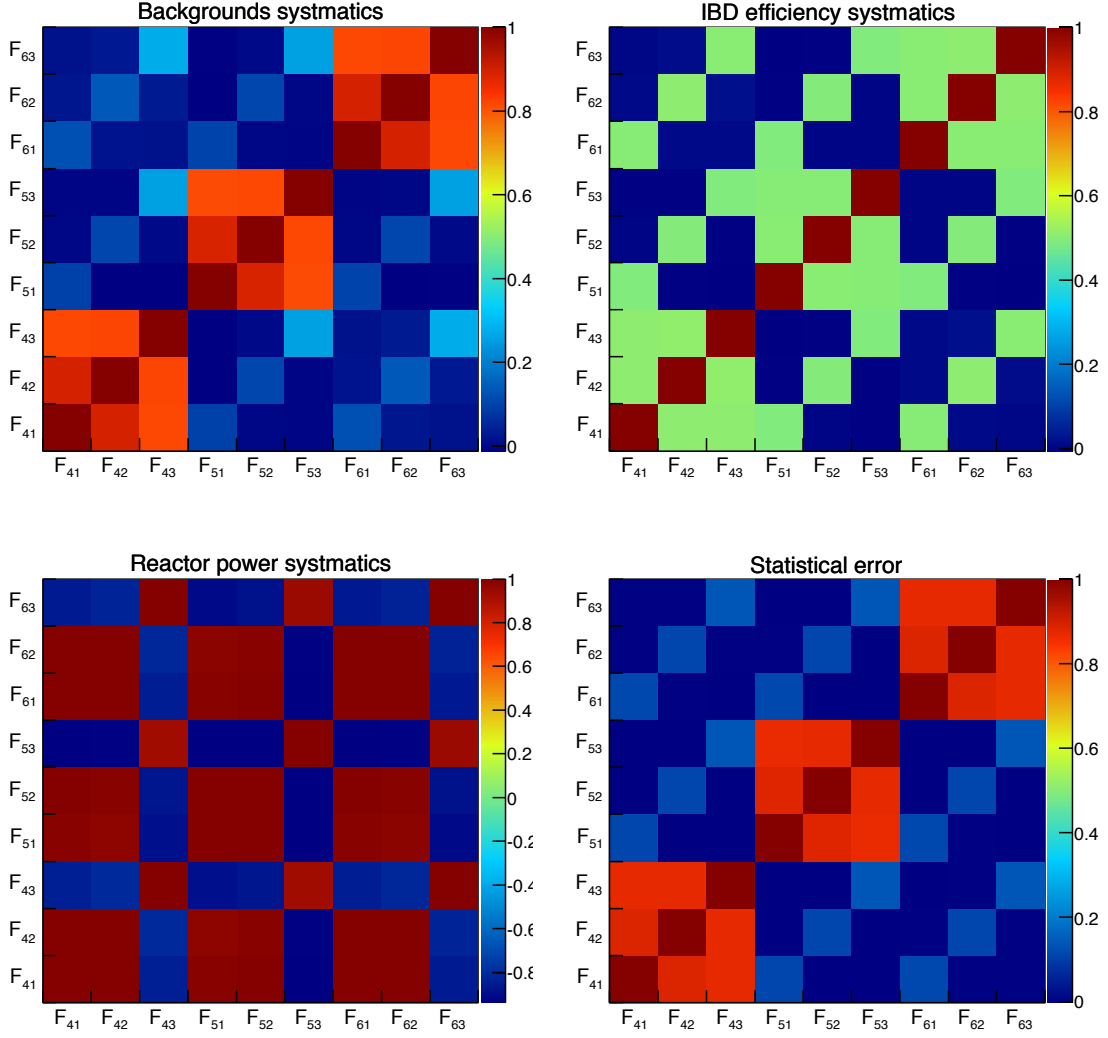
Figure 15: The size of the correlation $(V_{ij}/\sqrt{V_{ii}V_{jj}})$ in the covariance matrix for each error sources. The uncertainties for Background estimation (top left), IBD selection efficiency (top right), relative reactor power variation (bottom left) and statistics (bottom right) are shown.
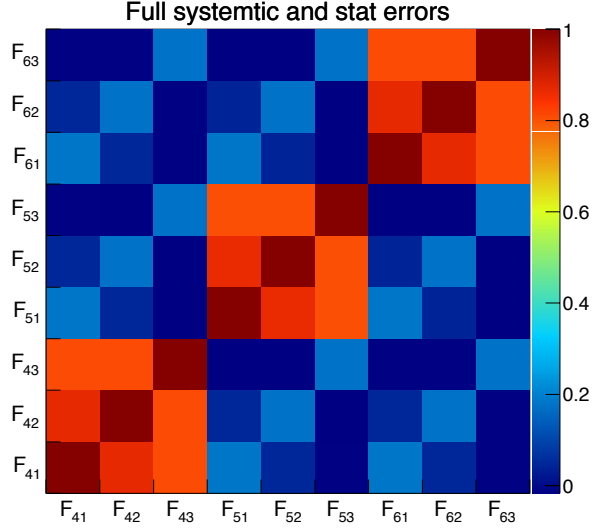
Figure 16: The size of the correlation $(V_{ij}/\sqrt{V_{ii}V_{jj}})$ in the covariance matrix for the full systematic and statistical uncertainties.

At this point it should be noted that the large correlation observed between elements suggests that there is no gain in sensitivity by treating these samples separately. Because of this, instead of fitting the nine variables, we consider only two that encapsulate most of the information:

$$F_{DB} = F_{4,1} + F_{4,2} + F_{5,1} + F_{5,2} + F_{6,1} + F_{6,2} \tag{15}$$

$$F_{LA} = F_{4,3} + F_{5,3} + F_{6,3}. \tag{16}$$

A 2×2 covariance matrix is thus constructed by adding the corresponding elements in the previous 9×9 matrix, and is used in the similar way. The results show that the sensitivity obtained with the reduced matrix have the same sensitivity as the larger one, as expected. Given that we fit two numbers (F_{DB} and F_{LA}) using one fit parameter ($\sin^2(2\theta_{13})$), we expect the number of degrees of freedom to be one ($= 2 - 1$).We confirmed this using toy MC samples produced with $\sin^2(2\theta_{13}) = 0.093$. Figure 17 shows the χ^2 distribution for the true $\sin^2(2\theta_{13})$ value, 0.093 (i.e. before making a fit.). We found the mean value of the χ^2 to be 1.96, which is consistent with the expectation from two degrees of freedom. This confirms that the covariance matrix is adequately representing the variation of the toy MC sample. Likewise, Figure 18 shows the χ^2 distribution for the best fit value for each toy MC sample. We found the mean value of the χ^2 is 0.98, which is, again, consistent with the expectation from one degrees of freedom.

8.2   Performance Tests

The performance of the fitting code was tested with the toy MC samples. Figure 19 illustrates the results that are obtained when the fitter is applied on toy MC samples with a true $\sin^2(2\theta_{13})$ of 0.005 and of 0.15. As can be seen there, the fitter was able to find the correct value of $\sin^2(2\theta_{13})$ in these two cases. It should be noted that the fitter does not allow negative values of θ_{13}. Because
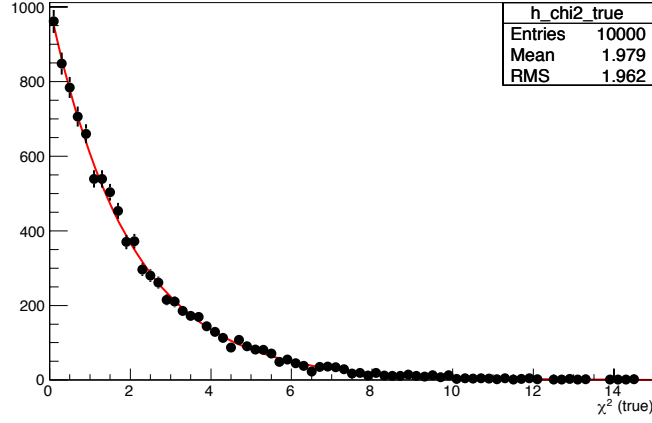
25

Figure 17: Distribution of χ^2 value for true $\sin^2(2\theta_{13})$ value (0.093). The black points show the result for each toy MC sample, and the red curve shows the expected χ^2 distribution with $NDF = 2$.
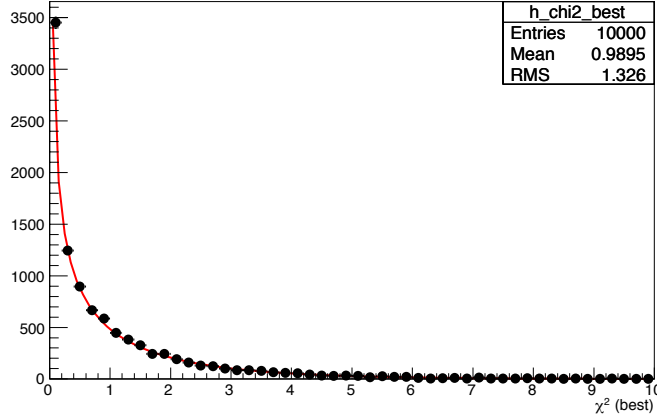

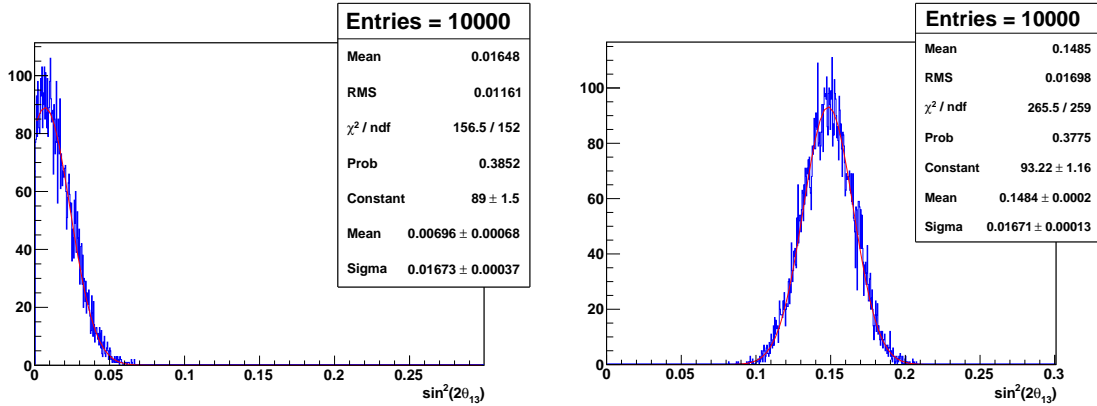Figure 18: Distribution of χ^2 value for the best fit $\sin^2(2\theta_{13})$ value for each toy MC sample. The black points show the result for each toy MC sample, and the red curve shows the expected χ^2 distribution with $NDF = 1$.

Figure 19: Fit results of 10,000 fake experiments with true $\sin^2(2\theta_{13}) = 0.005$ (left) and true $\sin^2(2\theta_{13}) = 0.15$ (right). A simple gaussian fit is applied in both cases.

of this, best fit values pile-up near $\sin^2(2\theta_{13}) = 0$, but on the positive side, whenever we are near the physical boundary.

Figure 20 presents the fitter's performance for all values of $\sin^2(2\theta_{13})$ between 0 and 0.3. In general, the fitter performs well for the values of $\sin^2(2\theta_{13})$ that are of interest to this analysis. The deviation of the mean best fit values from the $y = x$ curve that occurs near the physical boundary is to be expected, given the reasons explained above. The deviation that begins around $\sin^2(2\theta_{13}) \sim 0.25$ and which continues with increasing θ_{13} indicates that a slight discrepancy exists between the toy MC code and the fitter. This discrepancy is still under investigation, although it is not believed to be a major cause of concern, given that it appears at higher values of $\sin^2(2\theta_{13})$ only and it is quite small. Similar conclusions can be drawn for the RMS plot.
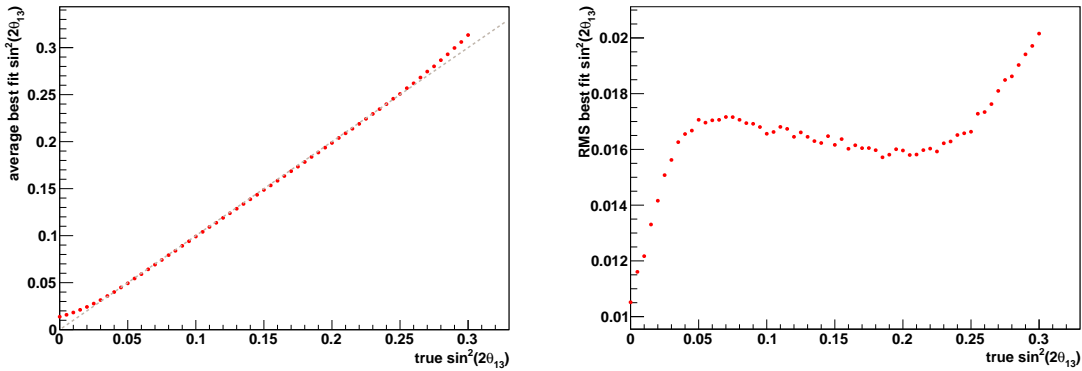

Figure 20: Fit results for true values of $\sin^2(2\theta_{13})$ between 0 and 0.3. On the left is the mean of the best fit values for each true $\sin^2(2\theta_{13})$, while on the right is the corresponding RMS vs. true $\sin^2(2\theta_{13})$. The dashed line on the left corresponds to the $y = x$ curve.

9   Analysis results

9.1   Best fit values

After validating the fitter against the toy MC samples and confirming that the method worked as expected, the machinery was applied to the real data. The results can be seen in Figure 23. Using all the data from the period of Dec. 24 2011 to Feb. 17 2012, and all the unblinded inputs, we find a best fit value and uncertainty of $\sin^2(2\theta_{13}) = 0.0932^{+0.0170}_{-0.0170}$ (stat+sys). This uncertainty is based on the values of $\sin^2(2\theta_{13})$ at $\Delta\chi^2 = 1$ (see next section for more details). The χ^2 at the best fit point is extremely good, of 0.005. Getting such a good χ^2 is not extremely unusual however, based on the toy MC samples. In fact, the probability of obtaining a χ^2 of 0.005 or higher assuming 1 degree of freedom is 0.944.

Table 17 summarizes the results in terms of the observed and expected number of events. A deficit in the number of events is clearly observed, which fits well to the oscillation hypothesis. It should be noted that, when considering the inverted hierarchy, the best fit value shifts to $\sin^2(2\theta_{13}) = 0.0937$, i.e. by $\sim 0.6\%$ only. Because of this the two hierarchies are not distinguished and the results reported throughout this note are for the normal hierarchy only.
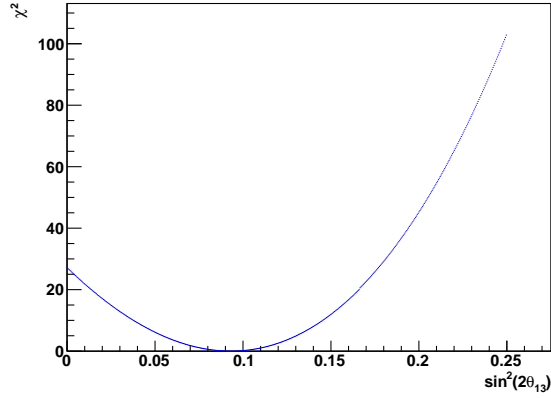
Figure 21: Results of the fit to the data from Dec. 24 to Feb. 17, using all the unblinded inputs. The best fit value is $\sin^2(2\theta_{13}) = 0.0932$ and the best fit χ^2 is 0.005.

	AD4			AD5			AD6		
Expected from	AD1	AD2	AD3	AD1	AD2	AD3	AD1	AD2	AD3
No oscillations	75.86	75.14	75.15	75.73	75.01	75.025	75.36	74.64	74.65
Best fit θ_{13}	71.37	70.67	71.07	71.24	70.55	70.94	70.89	70.20	70.59
Data	71.84 ± 1.27(stat)			70.09 ± 1.26(stat)			70.55 ± 1.26(stat)		

Table 17: Observed and expected number of events in each of the far ADs, in the case of no-oscillations and for the best fit θ_{13}. All numbers are normalized to one day of livetime and to the target mass of AD1.

9.2 Uncertainty in the Measurement

9.2.1 Systematic Uncertainties

Getting a qualitative feel of the systematic uncertainties from the covariance matrices is a straight-forward task. It suffices to look at the fractional size of the diagonal elements ($\sqrt{V_{ii}}$), as shown in Fig. 22. As expected, the dominant uncertainty is the statistical error, and the IBD efficiency systematics are a far second. This can also be seen in the $\Delta\chi^2$ distributions. Figure 23 and 24 show the $\Delta\chi^2$ values as a function $\sin^2(2\theta_{13})$ for the various sets of covariance matrices. The $\Delta\chi^2$ distribution does not change so much by subtracting systematic uncertainties. However, the distribution becomes much narrower when the statistical uncertainty is removed and the fit is done only with the systematic uncertainties. Among the systematic uncertainties, we can see from Fig. 24 that the dominating sources of error for the θ_{13} measurement are the IBD efficiency uncertainties and the uncorrelated reactor variations.
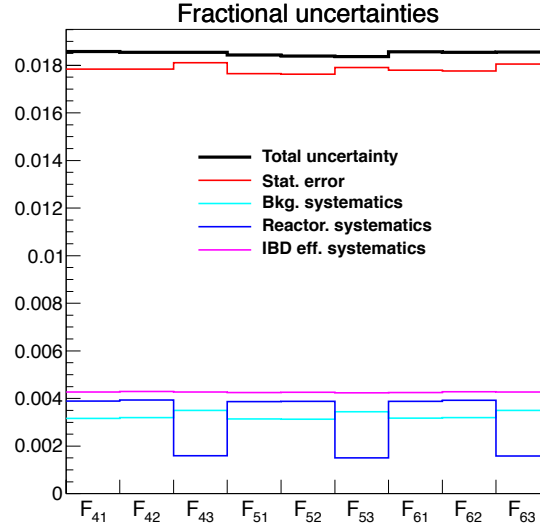

Figure 22: The fractional size of the diagonal elements ($\sqrt{(V_{ii}}$) of the covariance matrix.

In order to construct the systematic error budget we look at the variation in the best fit $\sin^2(2\theta_{13})$ for a toy MC sample where only one source of uncertainty is considered. The results of this are summarized in Table 18, for a $\sin^2(2\theta_{13})$ equal to the best fit value of 0.093. Figure 25 illustrates how the situation changes for a different value of $\sin^2(2\theta_{13})$. As expected, the errors are smallest at $\theta_{13} = 0$, due to the presence of the physical boundary which causes pile-up near it (and thus a reduction in the RMS). Also, for values of θ_{13} far away from the boundary, the errors tend to decrease with increasing θ_{13}. This is also expected due to the fact that the errors decrease with increasing oscillation signal.

A special mention should be made of the error due to the uncertainties in the reactor flux. For an absolute measurement, and for a core-to-core variation of 0.8%, a systematic error in the far site relative rate of $0.8/\sqrt(6) \sim 0.3\%$ is expected. Due to the fact that we are performing a
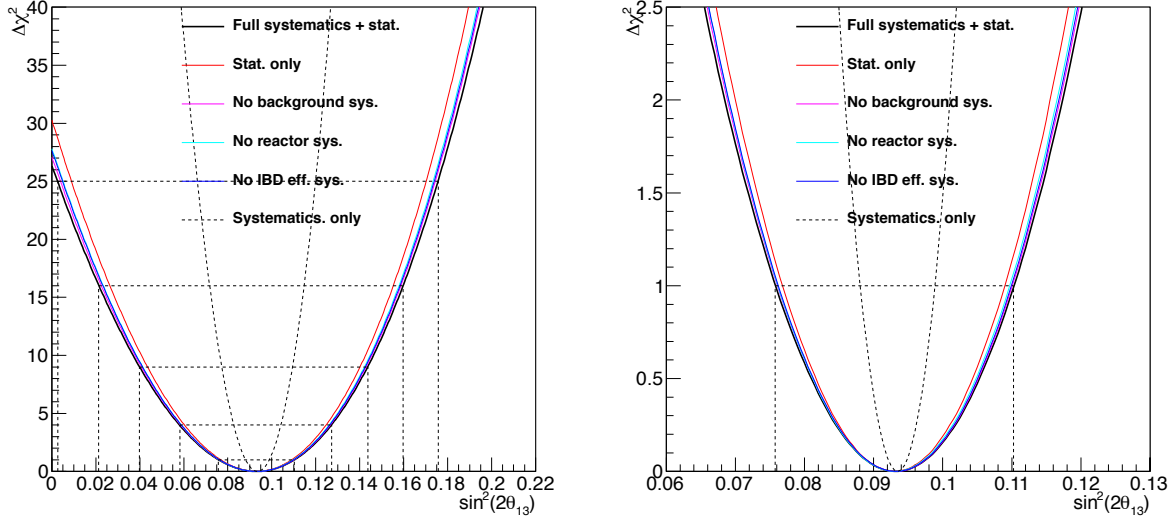
Figure 23: $\Delta\chi^2$ distribution as a function of $\sin^2(2\theta_{13})$. The results for full uncertainty, full uncertainty without background, reactor, IBD selection uncertainties, stat. only uncertainty and systematic only uncertainty are shown. The dashed lines indicate intersections at $\Delta\chi^2 = 1$, 4, 9, 16 and 25 for the full error matrix fit. The left and the right plots are same but show different $\sin^2(2\theta_{13})$ scale.
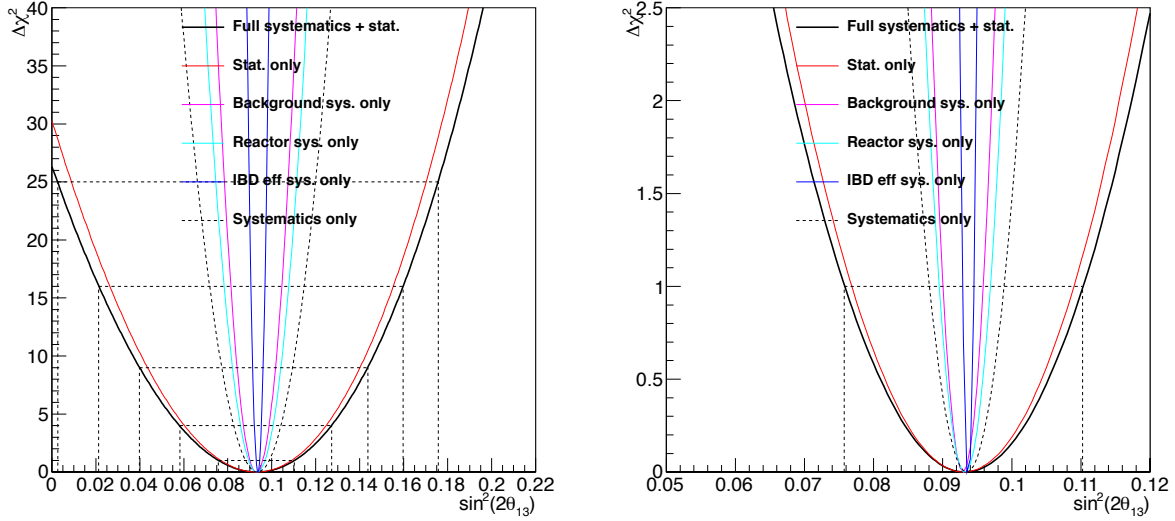

Figure 24: $\Delta\chi^2$ distribution as a function of $\sin^2(2\theta_{13})$ for each individual source of uncertainty. The results for full uncertainty, background, reactor, IBD selection uncertainties only , stat. only uncertainty and systematic only uncertainty are shown. The dashed lines indicate intersections at $\Delta\chi^2 = 1$, 4, 9, 16 and 25 for the full error matrix fit. The left and the right plots are same but show different $\sin^2(2\theta_{13})$ scale.
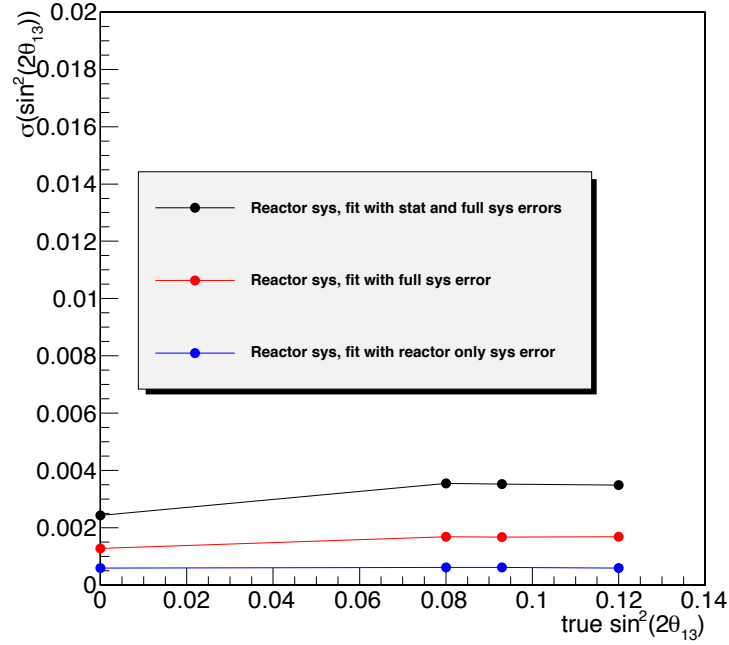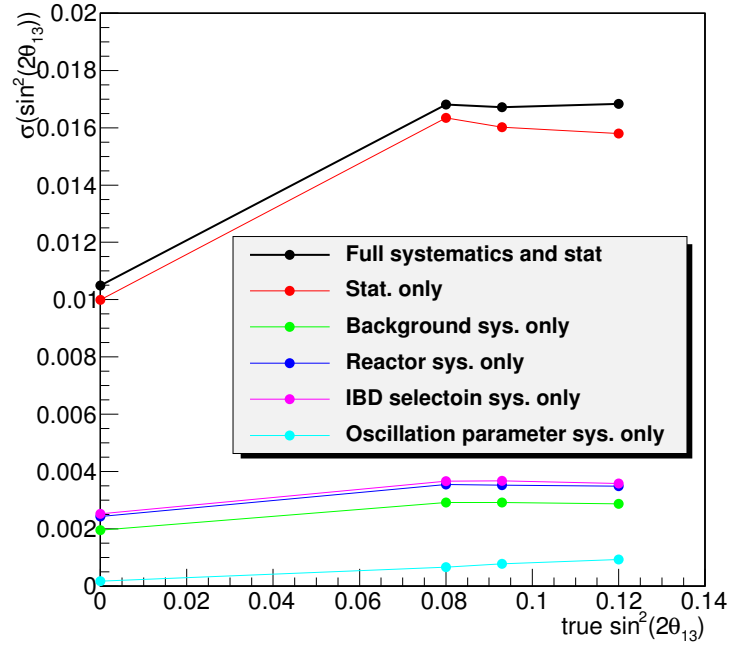
Figure 25: Left: 1σ statistical and systematic error budget for our measurement, for toy MC samples produced with various values of $\sin^2(2\theta_{13})$. Right: 1σ systematic error in our measurement due to reactor uncertainties, under the current statistics and under infinite statistics.

Reactor	IBD Efficiency	Background	Oscillation Parameters	Total Systematics
0.0035	0.0037	0.0029	0.0008	0.0059

Table 18: 1σ systematic error budget for our measurement of $\sin^2(2\theta_{13})$. The numbers are estimated from the RMS of the best fit $\sin^2(2\theta_{13})$ distribution that results from the application of the fitter to toy MC samples where only one of each of the sources of systematic error is considered. The toy MC samples used here are produced with a true $\sin^2(2\theta_{13})$ equal to the best fit value.

relative measurement, much of this should cancel. In fact, based on the numbers reported at the TDR, a $\sim 0.04\%$ relative rate uncertainty at the far site should result from a 0.8% uncorrelated reactor power uncertainty. This number corresponds to ~ 0.0006 when expressed in terms of the uncertainty in $\sin^2(2\theta_{13})$.

As just shown however, our current estimate for the reactor systematic error, in terms of $\sin^2(2\theta_{13})$, lies at 0.0035, which appears to be too high. It is interesting to note however that a reduction in this number is expected with increased statistics, as shown on the right side of Figure 25. The reason for this is that, the larger the statistical uncertainty, the harder it is for the fitter to separate the reactor effects from all others, including the oscillation signal. In fact, the same reasoning can be applied to all variations. Hence, as also shown in Figure 25, the reactor error would be reduced to 0.0006 if no other systematic errors existed, which is roughly consistent with the TDR expectation.

9.2.2 Total Error Estimation from a Feldman-Cousins Approach

When considering confidence intervals beyond 1σ, it is useful to cross-check the confidence intervals resulting from the covariance matrix method with a method that is known to work under all special circumstances, such as the proximity to a physical boundary. The method introduced by Feldman-Cousins[28] is thus a natural choice, particularly given the fact that we have a well-developed infrastructure to manufacture toy MC samples. Moreover, as shown below, the pursuit of this endeavor also enables us to make a statistically accurate statement concerning the confidence level at which $\theta_{13} = 0$ is excluded.

The implementation of our Feldman-Cousins approach is summarized by the scheme shown in Figure 26. We divide the $\sin^2(2\theta_{13})$ parameter space into a grid, from 0 to 0.3 in steps of 0.005. At each grid point, and for each fake experiment, the difference is taken between the χ^2 obtained using the θ_{13} of the given grid point, with the minimum χ^2 obtained in the fit. This difference is then used to fill a $\Delta\chi^2$ distribution which is studied to determine the limit L at which $x\%$ of fake experiments are excluded, as illustrated in Figure 27. The limits L are then compared to the $\Delta\chi^2$ resulting in the obtention of properly calculated confidence intervals.

The results obtained with this method are shown in Figure 28. Two comments are in order:

- The $1\sigma, 2\sigma$ and 3σ exclusion limits fall where expected when away from the physical boundary, i.e. at $\Delta\chi^2 = 1, 4$ and 9 respectively.

- The $1\sigma, 2\sigma$ and 3σ exclusion limits deviate from a straight line in the proximity of the physical boundary. This is not a surprise, given that one of the advantages of the Feldman-Cousins approach is precisely that it can correctly account for the presence of physical boundaries
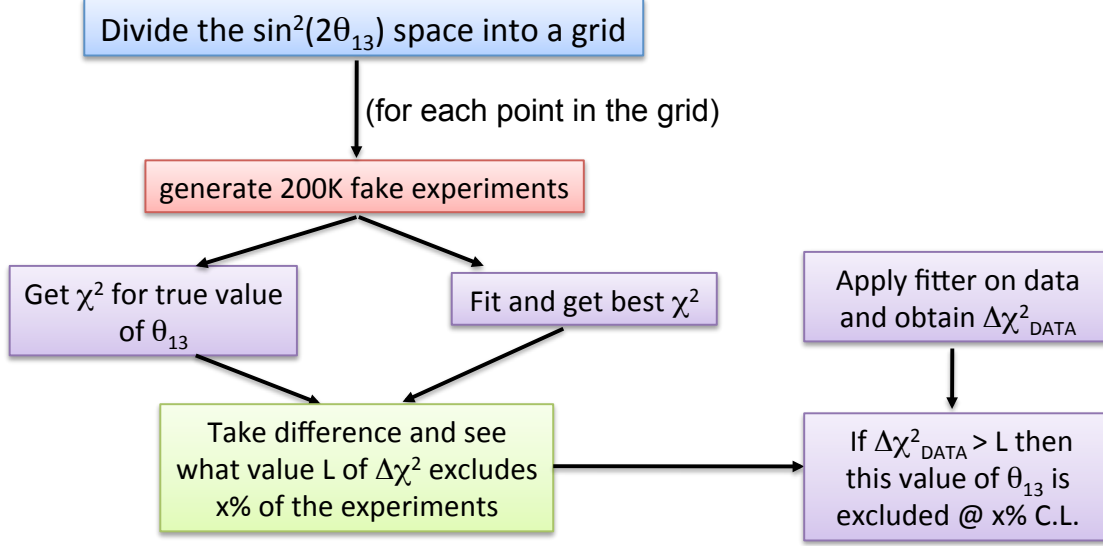
Figure 26: Scheme showing our Feldman-Cousins implementation.

Exclusion limit	Lower boundary	Higher Boundary
1σ	0.0761	0.111
2σ	0.0586	0.127
3σ	0.0417	0.143

Table 19: Confidence intervals in $\sin^2(2\theta_{13})$ derived with the Feldman-Cousins approach. As a reminder, the best fit value is $\sin^2(2\theta_{13}) = 0.093$. These boundaries are essentially the intersections between the $\Delta\chi^2$ from the data and the various exclusion limits of Figure 28.

when deriving confidence intervals, something that cannot be done in the simple Gaussian approximation. In this regard, it is particularly interesting that the limits derived with the Gaussian approximation are already slightly incorrect at the 3σ-level, and higher. By properly accounting for the presence of the physical boundary we are able to get more restrictive confidence intervals.

The limits in $\sin^2(2\theta_{13})$ derived from the Feldman-Cousins approach are compiled in Table 19. At the 1σ level, the result , i.e. $\sin^2(2\theta_{13}) = 0.0932^{+0.0170}_{-0.0171}$(stat. + syst.), is essentially the same as that obtained with the full covariance matrix. As the significance increases however the confidence interval becomes slightly less symmetric and the differences increase. The Feldman-Cousins contours constitute a more rigorous computation of our total error. Therefore, we take the total error as obtained from the Feldman-Cousins method, and we estimate the statistical contribution to it by subtracting the systematic error (in quadrature) as estimated in the previous section. The result is $\sin^2(2\theta_{13}) = 0.0932^{+0.0159}_{-0.0160}$(stat.)$\pm0.0059$(syst.).

Of particular interest to our collaboration at this point is the question of whether or not $\theta_{13} = 0$ is excluded at the 5σ level. In order to answer that question, we prepared a 100M sample of toy MC experiments at $\theta_{13} = 0$ and applied essentially the same methodology. The resulting $\Delta\chi^2$ distribution is shown in Figure 29. The value of $\Delta\chi^2$ at $\theta_{13} = 0$ obtained with the data is 26.3. In the 100M toy MC sample, there are only thirteen fake experiments with a $\Delta\chi^2$ equal
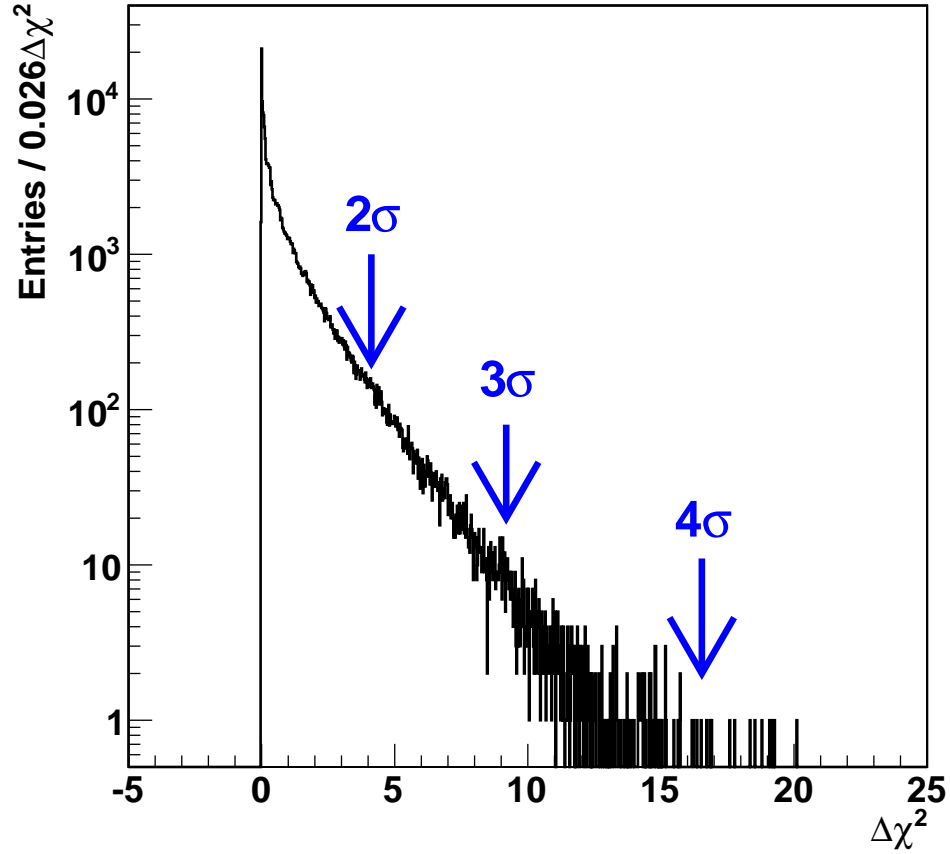
Figure 27: Example of the $\Delta\chi^2$ distribution obtained for a true $\sin^2(2\theta_{13})$ of 0.15. In this case, a cut at $\Delta\chi^2 = 1.05, 4.13, 9.2$ and 16.54 excludes 68.7%, 95.45%, 99.73% and 99.9937% of toy events (i.e. corresponds to $1\sigma, 2\sigma, 3\sigma$ and 4σ exclusion respectively). Note that obtaining exclusion limits at 5σ would approximately necessitate a ten-fold increase in the statistics at each grid point, and that the current statistics do not allow to obtain smooth contours at 4σ.
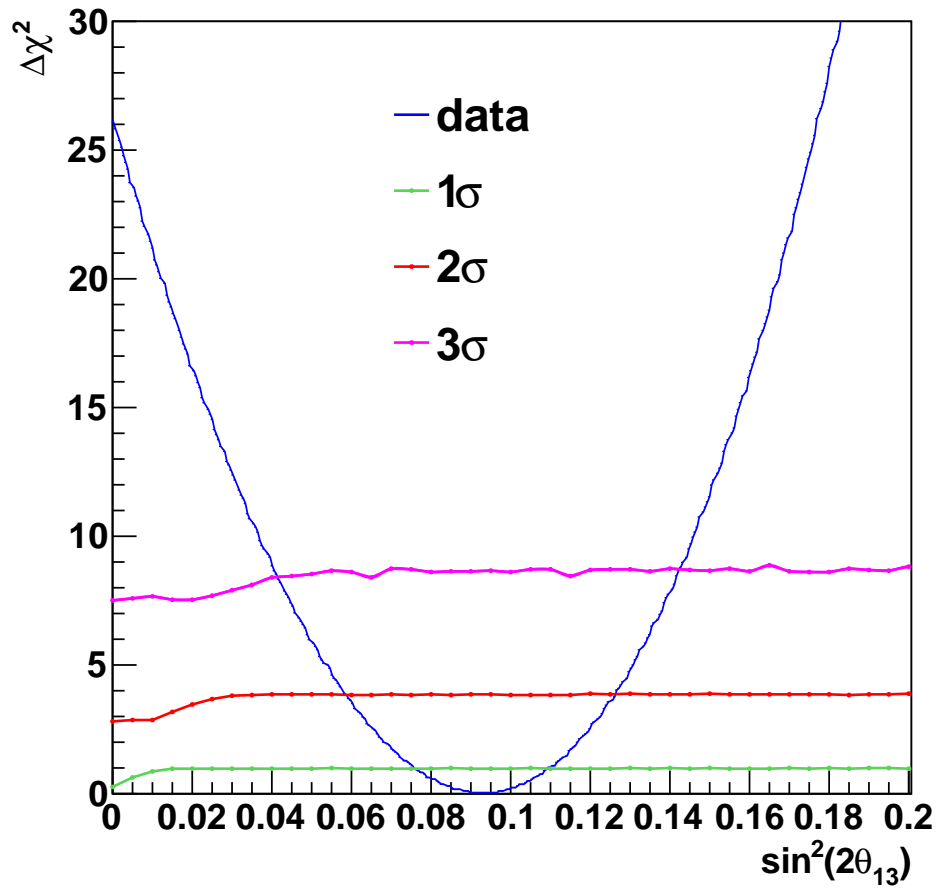
Figure 28: Results obtained with the Feldman-Cousins method. The $\Delta\chi^2$ obtained from the data is shown in blue. The other curves are the values of $\Delta\chi^2$ that exclude the fake experiments at $1\sigma, 2\sigma$ and 3σ respectively. Points along the blue curve that lie above the curves corresponding to a given limit are excluded with that confidence.

to or larger than this value, whereas if our result excluded $\theta_{13} = 0$ at exactly 5σ there should be $5.7 \times 10^{-7} \times 100\text{M} \sim 57$. Consequently, we conclude that we are well above 5σ significance. To exactly pinpoint the level of exclusion significantly more statistics would be required. It suffices to say to note for now that the p-value is approximately 2×10^{-8}.
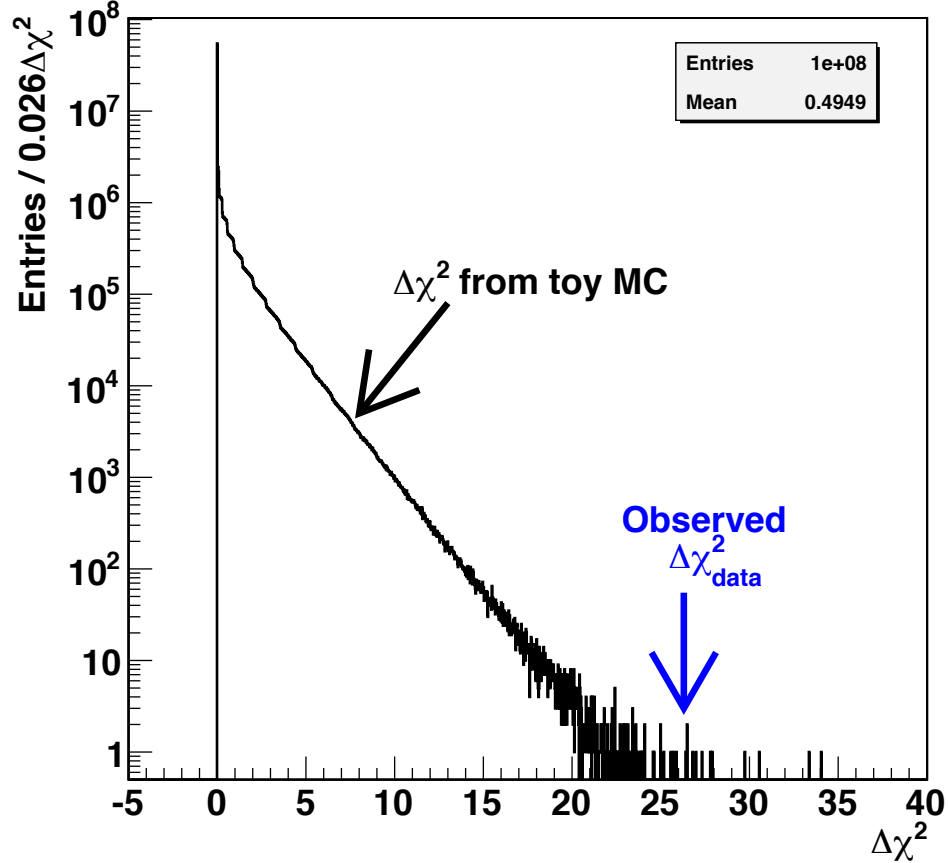

Figure 29: $\Delta\chi^2$ distribution for a 100M toy MC sample produced with a true $\theta_{13}=0$ and incorporating all the sources of systematic uncertainty. The p-value for a fake experiment to fluctuate to a value of $\Delta\chi^2 = 26.3$ or greater is about 1.3×10^{-7}.

10 Conclusions

We have performed a measurement of $\sin^2(2\theta_{13})$ with the Daya Bay three-site dataset from December 24th 2011 to February 17th 2012. We opted for a relative measurement, which allows for the automatic cancellation of all the correlated systematic uncertainties. All of the quantities involved in the analysis were independently estimated, with the exception of the smaller background components. The fit to θ_{13} was done using a covariance matrix approach, and the resulting confidence intervals were obtained with a Feldman-Cousins implementation. Our result, under the assumption of normal neutrino mass hierarchy, is $\sin^2(2\theta_{13}) = 0.0932^{+0.0159}_{-0.0160}(\text{stat.})\pm0.0059(\text{syst.})$.

11   Acknowledgements

We would like to thank Kam-Biu Luk and Herb Steiner for their encouragement and support, as well as for many valuable discussions in which they participated and which undoubtedly helped to make this analysis better. Likewise, we would also like to thank Dan Dwyer, Milind Diwan, Bryce Littlejohn and Matt Kramer for their direct and indirect contributions to this analysis. Finally, we would like to thank the other analysis groups, and the BCW group in particular, whose work gave us a model on which to build the first part of this analysis.

References

[1] Fengpeng An, "Reactor Neutrino Flux Prediction and Uncertainties", DocDB-7580.

[2] Jun Cao *et al.*, "Blind Analysis Policy", DocDB-7637.

[3] Christine Lewis, "Unblinded AD1-6 Target Masses", DocDB-7714.

[4] Matt Kramer *et al.*, "Progress on θ_{13} analysis", DocDB-7634.

[5] Matt Kramer *et al.*, "A Comparison of numbers for the Berkeley θ_{13} analysis", DocDB-7615.

[6] Dan Dwyer *al.*,"BCW θ_{13} Oscillation Analysis", DocDB-7621.

[7] C.-J. Lin *et al.*, "The AdSimple Reconstruction" , DocDB-7334.

[8] Yasuhiro Nakajima, "Vertex Reconstruction Using Charge Templates for AdSimple Reconstruction Package", DocDB-7536.

[9] Xin Qian *et al.*, "P12B Flasher Check", DocDB-7677.

[10] Jun Cao *et al.*, "Summary of Flasher Cuts", DocDB-7191.

[11] Jiajie Ling *et al.*, "Thoughts on Decoupled Multiplicity Cut", DocDB-7280.

[12] Xin Qian and Fenfang Wu, "Note of How We Get Singles and Accidentals", DocDB-7679.

[13] Jiajie Ling, Xin Qian, and Chao Zhang, "Some Discussions about Event's Timing Separation", DocDB-7278.

[14] Jiajie Ling and Xin Qian "Quick Update of ^{9}Li/^{8}He Background", DocDB-7563.

[15] Jiajie Ling *et al.*, "Update on ^{9}Li/^{8}He Calculation", DocDB-7653.

[16] Jiajie Ling and Xin Qian, "Fast Neutron Study with P12A + P12B Data", DocDB-7539.

[17] Xin Qian and Fenfang Wu, "Estimation of Correlated Bg from ACUs", DocB-7568.

[18] Wenqiang Gu and Jianglai Liu, "AmC Background Note", DocDB-6779.

[19] Zeyuan Yu, "Alpha-n Background Study", DocDB-7509.

[20] Fengpeng An, Jun Cao, Liang Zhan "Reactor Neutrino Flux Analysis", DocDB-6687

[21] Hahn, A.A. et al. Phys. Lett. B 218 (1989) 365.

[22] K. Schreckenbach. et al. Phys. Lett. B 160 (1985) 325.

[23] P. Vogel et al. Phys. Rev. C 24 (Oct, 1981) 1543

[24] P. Vogel and John F. Beacom, Phys.Rev.D 60:053003 (1999).

[25] Christine Lewis, Wei Wang, Liang Zhan "Cross check the IBD cross sections used by different groups", DocDB-7654.

[26] Littlejohn, Nakajima, Ochoa and Tsang, "AdSimple Energy Scale Check and Uncertainty for 6 ADs", DocDB-7583.

[27] Bryce Littlejohn, "Absolute and Relative Energy Cut Efficiency Investigation", DocDB-7658.

[28] Gary J. Feldman and Robert D. Cousins, "A Unified Approach to the Classical Statistical Analysis of Small Signals", Phys. Rev. D 57, 38733889 (1998).